Chinese Chemical Letters 34 (2023) 107523

Contents lists available at ScienceDirect

Chinese Chemical Letters

journal homepage: www.elsevier.com/locate/cclet

Layered photocatalytic nanomaterials for environmental applications

Fang Chen, Yihe Zhang, Hongwei Huang*

Beijing Key Laboratory of Materials Utilization of Nonmetallic Minerals and Solid Wastes, National Laboratory of Mineral Materials, School of Materials Science and Technology, China University of Geosciences, Beijing 100083, China

ARTICLE INFO

Article history:
Received 20 December 2021
Revised 9 February 2022
Accepted 11 May 2022
Available online 16 May 2022

Keywords:
Layered photocatalytic nanomaterials
Layered perovskite oxides
Environmental applications
Photocatalytic oxidation
Photocatalytic reduction

ABSTRACT

The increasing pollution and human demand for a cleaner environment have made achieving the environmental sustainability a current research focus. As a "green" technology, semiconductor photocatalysis is of great significance to the environmental purification. Benefiting from the unique anisotropic crystal structure and electronic properties, layered photocatalytic nanomaterials show great potential for efficient photocatalytic environmental treatment. This review comprehensively summarizes the recent progress on layered photocatalytic nanomaterials for oxidation or reduction of pollutants in water and air along with the basic understanding of related mechanisms and developments in this field. First, the existing diversified layered photocatalysts are classified, and their different synthesis and modification strategies are discussed in detail to provide a comprehensive view of the material design that affects their photocatalytic performance. Subsequently, the extensive applications of the above-mentioned layered photocatalytic nanomaterials in environmental fields are systematically summarized, including photooxidation of water and air pollutants, and photoreduction of heavy metal pollutants, NO_3^-, BrO_3^- and CO_2. Finally, based on the current research achievements in layered photocatalysts for environmental remediation, the future development direction and challenges are proposed.

1. Introduction

Environmental deterioration (mainly of water and air) has always been an urgent issue in modern society. The current researches on wastewater treatment mostly focus on physical absorption, biodegradable organic matter and biological compounds removal [1,2]. However, due to the extremely low biodegradability and insufficient removal rate of traditional wastewater treatment technologies, the treatment of micropollutants that endanger the health of organisms, such as drugs, dyes, phenols, and heavy metals, are still far from fulfilling the requirements. In addition, air pollutants such as CO_2, SO_x and NO_x from the combustion of fossil fuels have been considered to cause the greenhouse effect, photochemical smog and even lung diseases [3,4]. Therefore, water remediation and air purification hold great urgency and broad prospects for the development of a clean and sustainable environment [5]. Since the 1980s, photocatalytic technique has developed rapidly due to its low cost, mild reaction conditions and low energy consumption [6–8]. The environmental purification technology based on photocatalysis pioneers the endeavors for sewage and air treatment. However, conventional metal oxides based semiconducting photocatalysts suffer from low conversion efficiency of solar to chemical energy and cannot be applied on an industrial scale. The TiO_2-based photocatalytic materials with the good chemical stability and environmental compatibility have been the most exhaustively researched photocatalysts [9,10]. Despite considerable development of the band structure regulation and surface chemical modification, due to its wide band gap (3.2 eV) that only respond to UV light and low quantum yield, the application of TiO_2 to large-scale environmental treatment is still completely uneconomical methods [11]. Materials scientists have been striving to find and develop more efficient semiconductor photocatalysts [12–14]. Among them, layered photocatalytic nanomaterials have gained extensive attention of the researchers due to their unique layered structure with large surface area and remarkable physiochemical properties, providing a new way for the design, optimization and mechanism research of photocatalysts in environmental purification [15].

In this review, we systematically summarize the recent reports on layered photocatalytic nanomaterials, and classify their different types into metal containing and metal-free layered photocatalytic materials for the degradation of pharmaceuticals and industrial micropollutants degradation, NO_x removal, CO_2 reduction and Cr(VI) reduction reactions bridging the similarities and differences between them based on the photocatalytic oxidation and reduc-

* Corresponding author.
E-mail address: hhw@cugb.edu.cn (H. Huang).

https://doi.org/10.1016/j.cclet.2022.05.037
1001-8417/

Fig. 1. Schematic illustration of layered photocatalytic nanomaterials for environmental applications.

tion reaction mechanism. Therein, we focused on the morphology engineering, surface modification and heterostructure construction strategies based on the unique layered structure to improve the photocatalytic activity of layered nanomaterials. Finally, the various environmental applications and the future development of layered photocatalytic nanomaterials have been prospected. As far as we know, this will be the first comprehensive review of the synthesis, modification and application of a full range of layered photocatalytic nanomaterials. The different parts covered in this review are shown in Fig. 1.

2. Metal-containing layered photocatalytic nanomaterials

As an important part of photocatalytic materials, metal-containing layered photocatalytic nanomaterials have received the most extensive research in environmental applications. They can be typically divided into the following types: layered perovskite oxides, layered bismuth oxyhalides, layered double hydroxides (LDH), MXene and transition metal dichalcogenides (TMDs, Table S1 in Supporting information).

2.1. Layered perovskite oxides

Layered perovskite oxides are widely used in the environmental field due to their semiconducting properties. The structure consists of alternate layered stacks of discontinuous perovskite slabs separated by the adjacent layers by weak electrostatic interactions [16]. These distorted perovskite-like structures are similar to the general ABO_3 type and have the ordered corner-sharing BO_6 units [17]. According to the stacking orientation of the ideal cubic perovskite structure layers, the layered perovskite oxides can be classified as (100), (111) and (110) types [18]. For the (100) type, Aurivillius phase with the general formula $(Bi_2O_2)(A_{n-1}B_nO_{3n+1})$ that are constructed by the alternating layers of $[Bi_2O_2]^{2+}$ and $(A_{n-1}B_nO_{3n+1})$ perovskite-like layers as the most well-known layered perovskite oxides is expected to exhibit efficient photocatalytic performance in environmental treatment (Fig. 2a), Bi_2WO_6 with a moderate bandgap of approximately 2.6 eV is a typical Aurivillius phase perovskite oxide and one of the most intensively researched materials in photocatalytic applications. The Bi_2WO_6 nanoplates incline to assemble into flower-like hierarchical structure. Wang *et al.* prepared the reduced graphene oxide wrapped Bi_2WO_6 composite, and the core-shell Bi_2WO_6@rGO exhibited outstanding photocatalytic activity in the degradation of Rhodamine B by forming strong interaction and efficient charge separation between Bi_2WO_6 and rGO (Fig. 2b) [19]. As a ferroelectric Aurivillius phase compound, $BiMoO_6$ has also been extensively and intensively studied. Our group synthesized the ultra-thin Bi_2MoO_6 nanosheets with strong ferroelectricity through combined CTAB-assisted hydrothermal method and corona poling post-treatment (Fig. 2c). The increase of catalytic sites and the enhancement of internal electric field synergistically increased the photocatalytic CO_2 reduction activity with a CO evolution rate of 14.38 μmol g^{-1} h^{-1} of the polarized Bi_2MoO_6 ultrathin nanosheets in the gas-solid system (Fig. 2d) [20]. As an effective route to promote the charge separation of particle ferroelectric photocatalysts, the corona poling has been successfully applied to another typical Aurivillius phase layered niobate perovskite oxide based photocatalyst, $SrBi_2Nb_2O_9$ (Fig. 2e). Similarly, our group prepared the ferroelectric $SrBi_2Nb_2O_9$ nanosheets by an one-pot hydrothermal route. Due to its outstanding ferroelectric polarization and anisotropic charge transfer characteristics, $SrBi_2Nb_2O_9$ nanosheets possess highly efficient photocatalytic activity. Further, the ferroelectric polarization was enhanced through the 30 kV/cm electric poling or 400 °C annealing treatment, and the $SrBi_2Nb_2O_9$ nanosheets revealed an outstanding CH_4 evolution rate of 25.91 μmol g^{-1} h^{-1} with the apparent quantum efficiency (AQE) of 1.96% at 365 nm (Fig. 2f) [21].

The other two types of (100) series layered perovskite oxides are Ruddlesden-Popper (RP) phase and Dion-Jacobsen (DJ) phase with general formula $A_{n+1}B_nO_{3n+1}$/$A_2'A_{n-1}B_nO_{3n+1}$ (Fig. 3a) and $A'[A_{n-1}B_nO_{3n+1}]$ (Fig. 3b), respectively [22]. In Ruddlesden-Popper layered perovskite structure, the A and A′ are either alkali, alkaline-earth or rare-earth cations and there are the corners sharing BO_6 octahedra layers [23]. Sr_2TiO_4 and La_2NiO_4 are representative examples of RP layered perovskites and exhibit the strong photocatalytic ability to degrade pollutants. Sorkh-Kaman-Zadeh *et al.* synthesized the Sr_2TiO_4 nanostructures by a sono-chemical method with a good photocatalytic performance for degradation of toxic dyes (76%) in the presence of UV light [24]. A new nanostructure of La_2NiO_4 with hollow spherical morphology synthesized by the glycerol-assisted solvothermal approach was reported by Tao *et al.* Compared with the La_2NiO_4 nanosheets, the hollow-structured La_2NiO_4 spheres demonstrated a strong oxidation ability for organic pollutants (phenols and anionic dyes), and particularly a 87% removal rate of phenol in the dark within 12 h was achieved (Fig. 3c) [25]. $La_2Ti_2O_7$ is a characteristic DJ phase perovskite used for photocatalytic degradation of organic pollutants. Wang *et al.* reported that the Cr_2O_3/$La_2Ti_2O_7$ (14 wt% Cr_2O_3) p-n heterojunction exhibited high degradation activity for different pollutants under visible light irradiation, such as Rhodamine B and reactive brilliant red X-3B, which was due to the enhanced photoexcited charge separation and transfer [26]. The (111) and (110) series of layered perovskites oxide photocatalysts are represented by the general formulas $(A_{n+1}B_nO_{3n+3})$ and $(A_nB_nO_{3n+2})$, respectively, where *n* is the number of spanned corner-shared BO_6 octahedra in a layer (Figs. 3d and e) [27]. The weaker interlayer interactions in this type of structures allow facile exfoliation and heterocation substitution, which leads to increased surface area, wider light absorption range and faster charge transport. Iizuka *et al.* studied Ag loading on (111) layered perovskite $ALa_4Ti_4O_{15}$ (A = Ca, Sr and Ba) for photocatalytic CO_2 reduction into CO and HCOOH. The anisotropic structure of $BaLa_4Ti_4O_{15}$ contributed to the spatial separation of the oxidation and reduction reaction sites and the existence of the Ag cocatalyst specifically loading on the catalyst' edge, which led to its excellent photocatalytic activity (Fig. 3f) [28].

Layered perovskite oxide photocatalysts are typically synthesized by solid state reaction or hydrothermal methods. The use of tetra(*n*-butyl) ammonium hydroxide as the intercalation agent can easily exfoliate bulk layered perovskite oxides to yield ultra-thin

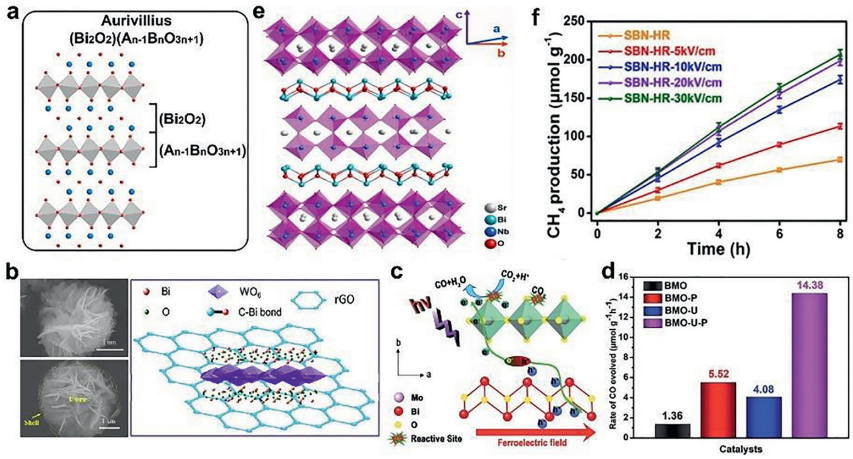

Fig. 2. (a) Crystal structure of Aurivillius layered perovskite oxides. (b) SEM images and formation of C-Bi bond of Bi_2WO_6@rGO. Reprinted with permission [19]. Copyright 2017, Elsevier. (c) The schematic illustration for the charge separation mechanism and CO_2 reduction reaction. (d) CO production rate over polarized ultrathin Bi_2MoO_6. Reprinted with permission [20]. Copyright 2020, Royal Society of Chemistry. (e) Crystal structure of $SrBi_2Nb_2O_9$. (f) Photocatalytic CH_4 production curves over $SrBi_2Nb_2O_9$ series samples annealed at 400 °C. Reprinted with permission [21]. Copyright 2021, Elsevier.

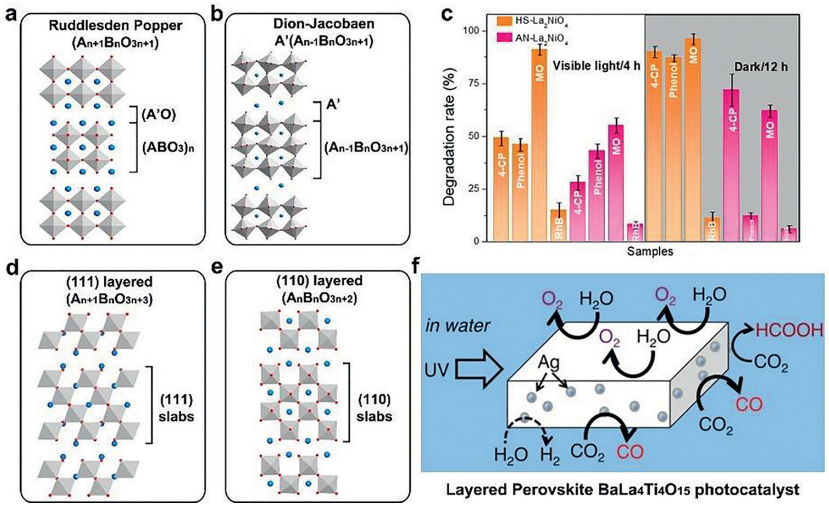

Fig. 3. (a) Crystal structures of Ruddlesden Popper, (b) Dion-Jacobaen, (d) (111) layered and (e) (110) layered perovskite oxides. (c) Degradation of various organic pollutants (4-CP, phenol, MO, RhB) by using hollow spheres La_2NiO_4 and aggregated nanoplate La_2NiO_4 as the catalyst under visible-light irradiation and in the dark. Reprinted with permission [25]. Copyright 2019, American Chemical Society. (f) Mechanism of photocatalytic CO_2 reduction over $BaLa_4Ti_4O_{15}$ with Ag cocatalysts loaded by several methods. Reprinted with permission [28]. Copyright 2011, American Chemical Society.

nanosheet structures with enlarged specific surface area and abundant reactive sites [29]. The two-dimensional (2D) structure of layered perovskite oxides has unique structural characteristics, which can provide the effective anisotropic charge transfer. In addition, most of the layered perovskites with a relatively wide band gap require band gap engineering to improve their light absorption properties. For example, uniform bulk nitrogen doping can redshift the band edge position and narrow the intrinsic wide band gap [30,31]. The layered crystal structure and anisotropic charge transfer endow the layered perovskite oxide photocatalysts with special photoelectronic and exciton transfer characteristics, and also enable a variety of possible modifications and performance adjustment strategies, making them interesting and showing great potential for various photocatalytic applications.

2.2. Sillén-phase bismuth-based photocatalysts

Bismuth oxyhalides, BiOX (X = Cl, Br and I) a typical Sillén-phase layered structure photocatalytic materials for environmental remediation, which is built by alternately stacked $[Bi_2O_2]^{2+}$ slabs and double halogen slabs with nonbonding (weak der Waals) interaction (Fig. 4a) [32,33]. The unique layered structure allows them suitable band structure and promising physicochemical properties such as chemical stability, non-toxicity, and corrosion resistance. Strong intralayer covalent bonds and weak interlayer van der Waals interactions favor the formation of the anisotropic structures of BiOX with (110) lateral facet and (001) top facet [34,35]. In addition, the exposure of anisotropic facets of BiOX can be easily controlled by regulating the synthetic environment and additives, which provides the possibility for crystal facet engineering to improve photocatalytic activity [36–38]. Our group prepared the eighteen-faceted BiOCl with (001) facets and (112) and (102) oblique facets through the one-pot hydrothermal method under long reaction time (100 h, Fig. 4b) [39]. Owing to the matchable band structure among the above three facets, a (001)/(102)/(112) ternary facet junction was formed, which provided a more effective cascade path of charge flow for spacial charge separation (Fig. 4c). Compared with the conventional (001)/(110) binary junction, the eighteen-faceted BiOCl displayed highly enhanced production of H_2 and hydroxyl radicals (•OH). As another feature of BiOX offered by

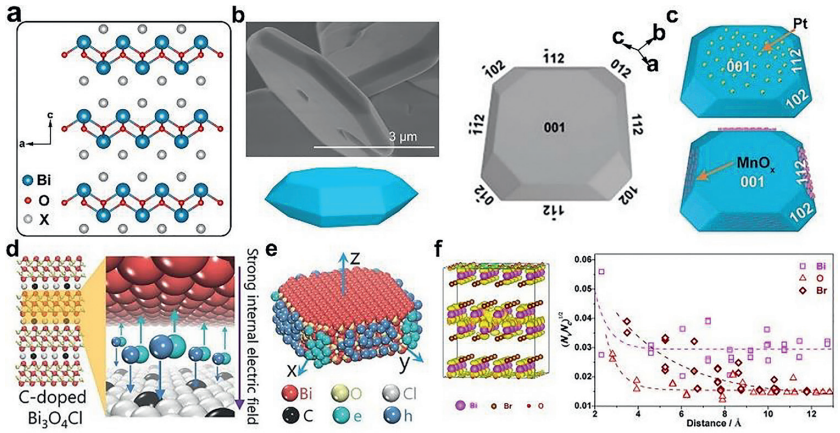

Fig. 4. (a) Crystal structure of BiOX (X = Cl, Br, I). (b) SEM images and the corresponding schematic representation for BiOCl-100. (c) The schematic representations for photodeposited BiOCl samples with Pt and MnO_x. Reprinted with permission [39]. Copyright 2019, Wiley-VCH. (d) Schematic illustration of the separation and (e) migration of electrons and holes in the bulk of C-doped Bi_3O_4Cl. Reprinted with permission [41]. Copyright 2016, Wiley-VCH. (f) The conduction charge density neat the band edges of the BiOBr model with oxygen vacancy and $(N_cN_v)^{1/2}$ value of atomic sites at different distances around the oxygen vacancy. Reprinted with permission [42]. Copyright 2018, American Chemical Society.

the unique layered structure, the internal electric field along the crystal orientation perpendicular to the $[Bi_2O_2]$ and [X] layers can provide a strong driving force for the separation of photogenerated electron-hole pairs [40]. Li *et al.* proved the effectiveness of carbon doping strategy for enhancing internal electric field by joint theoretical and experimental routes (Fig. 4d) [41]. The introduction of carbon increased the bulk charge separation efficiency to 80%, which strongly indicated that heteroatom doping is an effective way to control charge flow and improve photocatalytic performance (Fig. 4e). Compared with the introduction of foreign atoms, vacancy engineering provides another more convenient method to modulate the electronic properties and increase the charge separation. As an important type of lattice defects of BiOX photocatalysts, oxygen vacancies are qualitatively revealed through in-depth DFT calculations. Wang *et al.* analyzed the disordered redistribution of the band-edge charge states and the changes of localized valence states at different distances around the oxygen vacancy $(N_cN_v)^{1/2}$ (Fig. 4f), and first demonstrated that the introduced oxygen vacancies can significantly accelerate the dissociation of excitons, thereby enhancing the separation of charge carriers to efficiently participate in subsequent photocatalytic reactions (generation of superoxide radicals ($^{\bullet}O_2^-$) and synthesis of organic compounds) [42].

$BiOIO_3$ has a Sillén-related layered crystal structure consisting of $[Bi_2O_2]^{2+}$ layers interleaved with $[IO_3]^-$ trigonal pyramids (Fig. 5a). Due to the alignment of lone-pair containing polar IO_3 polyhedra, $BiOIO_3$ has a strong macroscopic polarity along the [001] direction [43]. Based on the above structural characteristics, our group synthesized single crystal $BiOIO_3$ nanostrips oriented along the [001] direction by controlling the pH during crystal growth process [44]. The morphology evolution of $BiOIO_3$ from nanoparticles (BIO-S) to nanostrips (BIO-L) allowed the catalyst an enhanced macroscopic polarization electric field, which provided a strong driving force for the separation of bulk charges (Figs. 5b and c). Further, by introducing oxygen vacancies on the surface, the photoinduced charges are driven to quickly migrate to the active sites on the surface of the $BiOIO_3$. Benefiting from the aforementioned bulk and surface co-polarization strategies, the efficient CO_2 reduction system was constructed, realizing a CO yield of 17.33 μmol g^{-1} h^{-1}. As another typical Sillén-related bismuth-based photocatalysts, $Bi_2O_2CO_3$ has a crystal structure similar to $BiOIO_3$ with alternative stacking of $(Bi_2O_2)^{2-}$ sheets interleaved by CO_3^{2-} groups [45]. The studies in recent years have shown that the exposure of (001) facets of $Bi_2O_2CO_3$ is beneficial to the improvement of photocatalytic activity, because the compression of Bi-O square anti-prism with 8-coordination along c-axis provides more oxygen defects to generate the electrons and holes [46,47].

The alternating layer structure composed of the Aurivilius phase and the Sillén phase consisting of the $[Bi_2O_2]^{2+}$ layers intergrown with the halide slabs is named the Sillén–Aurivilius structure. Bi_4MO_8X (M = Ta, Nb; X = Cl, Br), as the most representative Sillén–Aurivillius structured perovskite oxyhalides, has received extensive attention since the first discovery of Fujito *et al.* and our group (Fig. 5d) [48,49]. The Bi_4MO_8X plates with (001) exposing facets are usually prepared by a flux method [50]. For example, our group synthesized Bi_4NbO_8X (X = Cl, Br) monocrystalline nanosheets by the flux method using NaCl and KCl as the molten salt [51]. In view of their noncentrosymmetric crystal structure and strong light absorption in the visible light region, they are remarkable candidates for piezoelectric photocatalysis. The ultrasound-induced [001] oriented piezoelectric field and related band bending not only promoted the separation of photogenerated charges, but also enriched the reduction reaction sites on the surface of Bi_4NbO_8X to achieve high-efficiency evolution of reactive oxygen species by coupling piezocatalysis and photocatalysis (Figs. 5e and f).

With unique layered-structure mediated properties, such as pH-dependent crystal facet exposure, facet-dependent internal electric field intensity, *etc.*, the Sillén-phase bismuth-based nanomaterials are considered as one of the most promising photocatalysts in the environmental fields.

2.3. Layered double hydroxides

Layered double hydroxides (LDHs) are a group of anionic clay materials with layered structure, also known as hydrotalcite [52]. The general formula is $[M^{2+}_{1-x}M^{3+}_x(OH)_2]^{x+}(A^{n-}_{x/n})\cdot yH_2O$, where M^{2+} is divalent metal ion (Zn^{2+}, Mg^{2+}, Cu^{2+}); M^{3+} is trivalent metal ion (Al^{3+}, Cr^{3+}, Fe^{3+}); each metal cation on the slabs is bonded with the OH^- groups to form the framework of LDHs. A^{n-} are charge balancing anions including organic, inorganic and heteropoly-anions [53,54]. The crystal structure of LDHs is shown in Fig. 6a, where the layered structure is composed of two or more divalent or trivalent metal hydroxides, and the anions located in the interlayer maintain the stability of LDH by keeping the charge neutrality. According to application requirements, LDHs-based materials can have unique structure and photocatalytic properties by adjusting components such as the type of metal ions and interlayer anions [55].

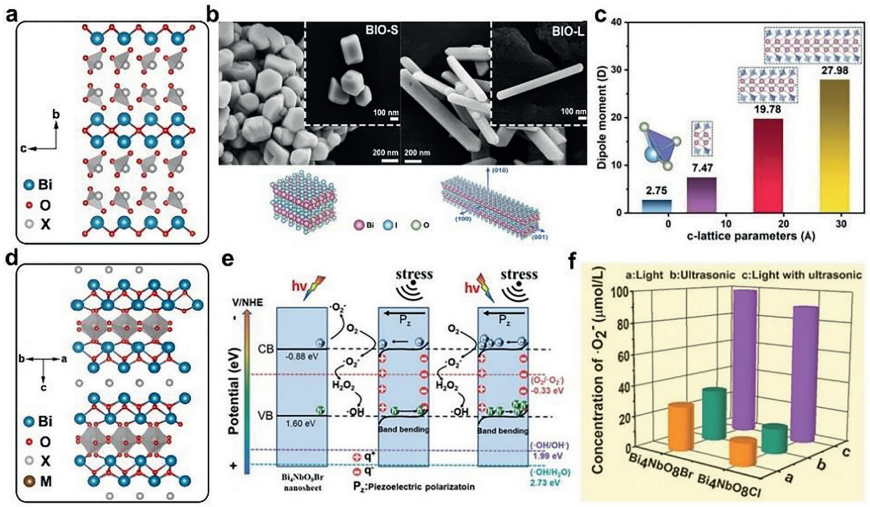

Fig. 5. (a) Crystal structure of $BiOIO_3$. (b) The morphology evolution and the corresponding schematic illustration for BIO-S and BIO-L. (c) The dipole moment (z-axis) of IO_3 polyhedra and the $BiOIO_3$ unit cells with different c-lattice lengths. Reprinted with permission [44]. Copyright 2020, Wiley-VCH. (d) Crystal structure of Bi_4MO_8X (M = Ta, Nb; X = Cl, Br). (e) Diagram of band bending of Bi_4NbO_8Br under different conditions. (f) The concentration of $^{\bullet}O_2^-$ over Bi_4NbO_8X (X = Cl, Br) under light, ultrasonic and simultaneous light and ultrasonic irradiation within 2 h. Reprinted with permission [51]. Copyright 2019, Wiley-VCH.

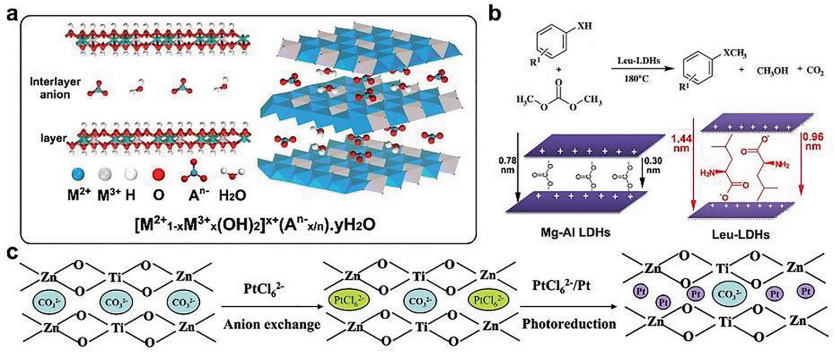

Fig. 6. (a) Structure of LDHs. (b) Leu-LDHs catalyzed chemoselective *O*-methylation of substituted phenols and thiophenols with DMC and the schematic structural models of Mg-Al LDHs and Leu-LDHs. Reprinted with permission [57]. Copyright 2013, Elsevier. (c) Schematic illustration for synthesis of nanoPt intercalated Zn-Ti LDHs composite (Zn-Ti LDHs; subsequent exchange of $PtCl_6^{2-}$ with anions of CO_3^{2-}; followed by photoreduction to form the assembly of Pt/Zn–Ti LDHs. Reprinted with permission [58]. Copyright 2014, Elsevier.

Due to the relatively weak interlayer bonding, LDHs exhibit remarkable ability to exchange interlayer anions. The high fluidity and exchangeability of the anions residing in the interlayer have important applications in improving photocatalytic activity [56]. The size and valence state of anions and the intensity of interlayer hydrogen bond network affect the interlayer spacing, electron density and band structure of LDHs, respectively, greatly affecting the photocatalytic performance. The interlayer spacing of LDHs can be adjusted by inserting amino acids with different physiochemical properties. Subramanian *et al.* intercalated sixteen different amino acids into Mg-Al LDHs by reconstruction methods with the increase in interlayer space of LDHs and found that the insertion of amino acids possessing a hydrophobic sidechain (Leu-LDHs) can effectively improve the photocatalytic degradation reactivity and selectivity of LDHs towards phenol degradation (Fig. 6b) [57]. As another typical example, Chen *et al.* inserted Pt containing organic ligands between the LDHs layer to synthesize Pt/ZnTi-LDHs photocatalyst through ion exchange, which showed a large specific surface area (111.46 m^2/g) and pore volume (0.317 cm^3/g, Fig. 6c) [58]. The modified LDHs displayed expanded photoresponse range and largely improved photoexcited charge separation and transport performance, thereby increasing the photodegradation of RhB.

Based on the layered configuration of LDHs, they can be exfoliated into positively-charged 2D nanosheets and oppositely-charged catalytically active species *via* layer-by-layer assembly [59]. So, Gunjakar *et al.* synthesized the mesoporous layer-by-layer ordered nano-hybrid with preeminent visible light photocatalytic activity through electrostatic self-assembly between positively-charged Zn-Cr-LDH nanosheets and negatively-charged layered titanate nanosheets (ZCT) [60]. The excellent photocatalytic O_2 production rate (~0.67 mmol h^{-1} g^{-1}) and chemical stability of the heterolayered nanohybrids were attributed to the electronic coupling between the two components and the protection of LDHs lattice by the layered titanate.

LDHs constitute a series of excellent photocatalytic materials, especially the photocatalysts driven by visible light, because they have an adjustable band gap ranging from 2.2 eV to 3.2 eV. In addition, the advantages of LDH such as low cost and facile synthesis make them closer to practical applications.

2.4. MXene

A large family of early transition metal carbides and/or nitrides with the layered structures is named "MXene", which has received widespread attention as a rapidly rising star in the field of photocatalysis [61,62]. MXene consists of $M_{n+1}X_n$ stacked slices. M is the transition metal, including Ti, Ta, Zr, Mo, *etc.* X represents the C or N elements held together by hydrogen

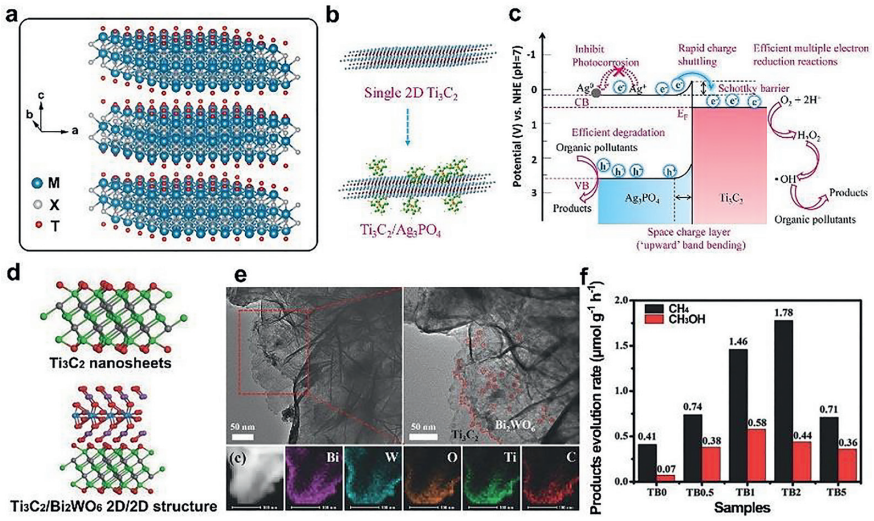

Fig. 7. (a) Crystal structure of MXene. (b) Schematic representation of single 2D Ti_3C_2 sheets and Ag_3PO_4/Ti_3C_2 synthesis. (c) The mechanism of photodegradation and anti-photocorrosion of Ag_3PO_4/Ti_3C_2 Schottky catalyst. Reprinted with permission [66]. Copyright 2018, Elsevier. (d) Schematic illustration of the synthetic of 2D/2D heterojunction. (e) TEM image of ultrathin Ti_3C_2/Bi_2WO_6 nanosheets. (f) Photocatalytic activity of TB0 to TB5. Reprinted with permission [67]. Copyright 2018, Wiley-VCH.

bonds or van der Waals interactions. At the same time, the surfaces of the MXene layers are typically terminated with OH, O and F. Thus, the general formula $M_{n+1}X_nT_x$ is generated, herein T_x represents the x surface terminating group (Fig. 7a) [63,64]. MXene has excellent structural stability, tunable bandgap (0.92-1.75 eV), ideal electronic structure, and efficient electrons and holes anisotropic mobility, becoming one of the most potential photocatalytic nanomaterials in environmental governance [65]. In general, most MXenes serve as co-catalysts in the photocatalytic reactions, and researchers use MXene to modify semiconductor photocatalysts to improve their rapid photoexcited carriers recombination, thereby increasing the quantum efficiency and photocatalytic activity. Among these modification strategies, MXene Schottky junction and heterostructure can effectively accelerate the photocatalytic performance by adjusting the electronic structure. Cai *et al.* successfully synthesized Ag_3PO_4/Ti_3C_2 Schottky junction catalyst by electrostatic self-assembly method (Fig. 7b) [66]. Due to the formation of sufficiently and closely contacted interface between the two phases Ti_3C_2 enhanced the photodegradation activity and photocorrosion resistance of Ag_3PO_4 by capturing the unidirectional electron flow across Schottky barrier (Fig. 7c). It can be observed that the photocatalytic performance of Ag_3PO_4/Ti_3C_2 for tetracycline hydrochloride has a relatively small loss after 8 cycles, which still maintained 68.4%. In addition, the high-efficiency photocatalytic reduction of Cr^{6+} over AgI/Ti_3C_2 system also strongly indicated that Ti_3C_2 as a versatile "electron sink" can be used in a wide range of environmental treatments. Another advantage of MXene as a co-catalyst is that it has a layered structure and abundant surface functional groups, which can provide favorable conditions for the construction of heterojunctions. Cao *et al.* fabricated the 2D/2D heterojunction by growing $BiWO_6$ nanosheets *in situ* on the Ti_3C_2 nanosheets (Fig. 7d) [67]. The ultra-thin structure and abundant terminal groups of Ti_3C_2 provided a large contact area and tight interface for the Ti_3C_2/Bi_2WO_6 heterojunction photocatalyst, which greatly improves the charge transfer capacity. Thus, Ti_3C_2/Bi_2WO_6 heterojunction demonstrated 4.6 times higher activity than that of primitive Bi_2WO_6 ultrathin materials for the photocatalytic production of CH_4 and CH_3OH, respectively (Figs. 7e and f).

Fabrication of MXene-based junction provides an effective route to construct a high-efficiency photocatalytic system, which is attributed to its stronger light absorption and faster charge transfer. In addition, the large specific surface area allows more reactive sites. The unique optical properties, electronic structure, stability and hydrophilicity make MXene widely concerned in its surface modification and application.

2.5. Transition metal dichalcogenides

Transition metal dichalcogenides (TMDs) such as MoS_2, $MoSe_2$ and WS_2 that consist of a hexagonal layer of metal atoms M sandwiched between two MX_2 stoichiometric chalcogen layers have attracted enormous research enthusiasm in the field of photocatalysis (Fig. 8a) [68,69]. Benefiting from its intrinsic layered structure and weak van der Waals interactions between layers, the bulk TMDs can be exfoliated into corresponding thin-layered nanosheets [70–72]. Koyyada *et al.* successfully prepared hexagonal WS_2 nanosheets (e-h-WS_2) with a narrow band gap and higher specific surface area through a liquid phase exfoliation process in dimethylformamide solution (Figs. 8b and c) [73]. Compared with the hexagonal WS_2 (h-WS_2), the monolayered or few-layered WS_2 (e-h-WS_2) nanosheets showed enhanced photocatalytic activity and excellent stability in the degradation of various organic dye pollutants under simulated solar light irradiation. In addition, the high anisotropy and unique crystal structure of TMDs make them widely used as co-catalysts for the modification of semiconductor photocatalysts [74,75]. The unique 2D layered structure of TMDs can be used as an effective support for the anchoring of semiconductor nanoparticles, allowing efficient charge separation, more dispersed active sites and stability [76]. Islam *et al.* synthesized heterodimensional nanostructures of ultrathin MoS_2 nanosheets (2D) uniformly intersperaed with ZnO nanoparticles (0D) by ultrasound-assisted and wet chemical processes (Fig. 8d) [77]. Benefiting from the rapid charge carriers migration between ZnO and MoS_2 with the intimate interface and the large adsorption surface, the optimized *quasi*-0D/2D hybrid nanomaterial exhibited excellent photocatalytic ability, which degraded more than approximately 90% of various organic dyes and tetracycline within 30 min. It is worth noting that nano-sized MoS_2 as the eminent O_2-activator for the oxidation reactions can boost the generation of $^{\bullet}O_2^-$ [78]. Guo *et al.* reported a structure-controlled nano-flower-like 3D microsphere photocatalyst with excellent photocatalytic activity (Fig. 8e) [79]. The abundant active-edge sites and unique physicochemical properties of MoS_2 nanosheets

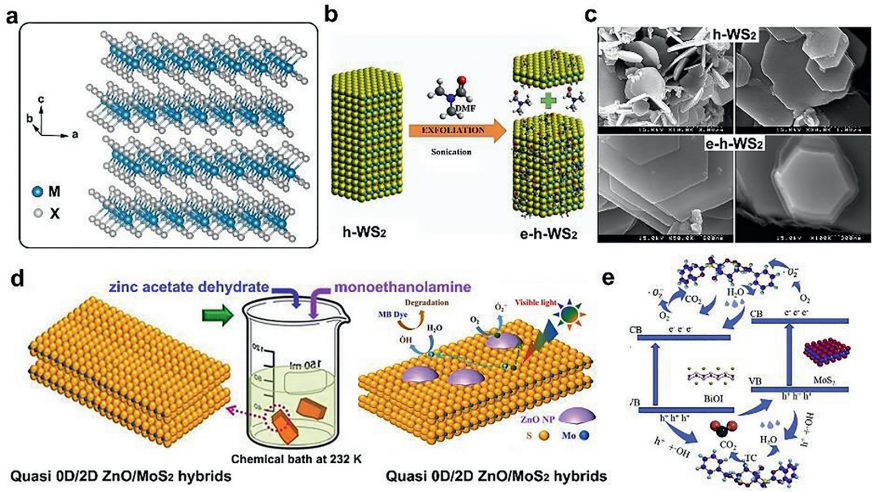

Fig. 8. (a) Crystal structure of TMDs with a typical formula MX_2. (b) scheme of exfoliation procedure for hexagonal WS_2 catalyst. (c) SEM images of h-WS_2 platelets and e-h-WS_2 platelets. Reprinted with permission [73]. Copyright 2019, Elsevier. (d) Schematic illustrations of a "bottom-up" wet chemical process to obtain heterodimensional ZnO/MoS_2 nanocomposites and the proposed photocatalytic mechanism under visible-light irradiation. Reprinted with permission [77]. Copyright 2018, Wiley-VCH. (e) Photocatalytic mechanism of the 3D BiOI/MoS_2 microspheres under visible-light irradiation. Reprinted with permission [79]. Copyright 2021, Elsevier.

enabled 3D BiOI/MoS_2 microspheres to show greatly inhibited recombination of photogenerated electrons and holes, achieving an optimum photocatalytic activity for degradation of methyl orange and tetracycline as high as 95.6% and 91.5% within 75 min, respectively.

The layered structure of TMDs can be used as an effective support for the anchoring of semiconductor nanoparticles. At the same time, by formation of heterojunction between TMDs nanosheets and semiconductors, more effective charge transfer can be achieved. A lot of pioneer work has found that their photocatalytic activity originated from active sites anchored at exposed and uncoordinated marginal sites. In view of these advantages, TMDs are expected to become one of the star materials to replace noble metals for co-catalysis.

3. Metal-free layered photocatalytic nanomaterials

In the "green" 21st century, compared with the high cost and easy corrosion of metal-based photocatalysts, metal-free layered photocatalysts nanomaterials have received extensive attention due to their abundant reserves, good durability and environmental sustainability. Metal-free layered photocatalytic materials can be divided into graphite carbon nitride, hexagonal boron nitride and black phosphorus (Table S2 in Supporting information).

3.1. Graphitic carbon nitride

Franklin prepared graphitic carbon nitride (g-C_3N_4) by the thermal decomposition of mercuric thiocyanate in 1922 [80]. After that, the investigation of g-C_3N_4 has begun. In the structure of g-C_3N_4, C and N atoms are connected by sp^2 hybridization with σ bonds to form a hexagonal structure, which is called a triazine ring. At the same time, the triazine ring is linked by the terminal N atom to form an extended layer structure. Compared with the *s*-triazine ring (C_3N_3), g-C_3N_4 with ordered tri-*s*-triazine units (C_6N_7) proves to be the most stable structure (Fig. 9a) [81]. The g-C_3N_4 as a metal-free polymer semiconductor photocatalyst was first reported by Wang *et al.* in 2009, which can realize photocatalytic water splitting to produce hydrogen [82]. This research opens a new direction for realizing the direct conversion of solar energy to chemical energy *via* metal-free photocatalyst. Meanwhile, due to the earth-abundant reserves, simple synthesis, moderate band gap (2.7 eV), ideal electronic structure and high stability of g-C_3N_4, it has become one of the most popular layered photocatalytic nanomaterials in the field of environmental pollution [83,84]. However, the photocatalytic activity of g-C_3N_4 is still limited in practical applications due to its low visible light absorption, small specific surface area, and high photogenerated electron and hole recombination efficiency [85].

Among various modification strategies for optimizing photocatalytic performance, as one of the simplest and most effective methods, element doping including alkali metals (Li, Na, K) [86,87], transition metals (Cu, Fe, W) [88,89] and non-metals [90] can ameliorate the environmental management of g-C_3N_4 photocatalyst by adjusting the electronic structure. Based on the layered structure of g-C_3N_4, Xiong *et al.* inserted K atoms into the interlayer of g-C_3N_4, which served as a transmission channel by bridging the layer, greatly improving the separation and transfer of photoexcited electron-hole pairs between adjacent layers [91]. Furthermore, the non-metal elements doping can continue the metal-free characteristics of g-C_3N_4, which breaks the symmetry of g-C_3N_4 by forming covalent bonds and results in the efficient separation of photogenerated charge carriers [92]. Zeng *et al.* successfully synthesized oxygen-doped g-C_3N_4 nanorods (*O*-g-C_3N_4) with a well-defined porosity (Fig. 9b) [93]. Compared with the original g-C_3N_4, the interplanar spacing of *O*-g-C_3N_4 nanofibers was expanded by 1.204 Å, which resulted in a larger specific surface area (114.2 m^2/g) and stronger spin strength (Fig. 9c). FT-IR and high-resolution XPS spectroscopy together proved the introduction of homogeneously distributed O atoms (Figs. 9d and e). In addition, the O doping expanded the band gap of g-C_3N_4 (Fig. 9f). Therefore, *O*-g-C_3N_4 showed improved light absorption capacity and charge separation efficiency and an excellent photocatalytic degradation ratio of 2,4-dinitrophenol.

Owing to the layered structure, thin-layer g-C_3N_4 nanostructures with p-conjugated system and appropriate energy band gap can be easily synthesized [94], which allows g-C_3N_4 a large specific surface area and short charge transfer distance, greatly promoting the applications of g-C_3N_4 in photocatalysis [95]. Li *et al.* weakened the van der Waals force between layers in the bulk g-C_3N_4 by a post-calcination method, and synthesized g-C_3N_4 nanosheets with a thickness of about 2 nm (Figs. 9g and h) [96]. The thin-layer g-C_3N_4 nanosheets are excellent in photodegradation of pollutants and hydrogen production (57.20 μmol/h), which is attributed

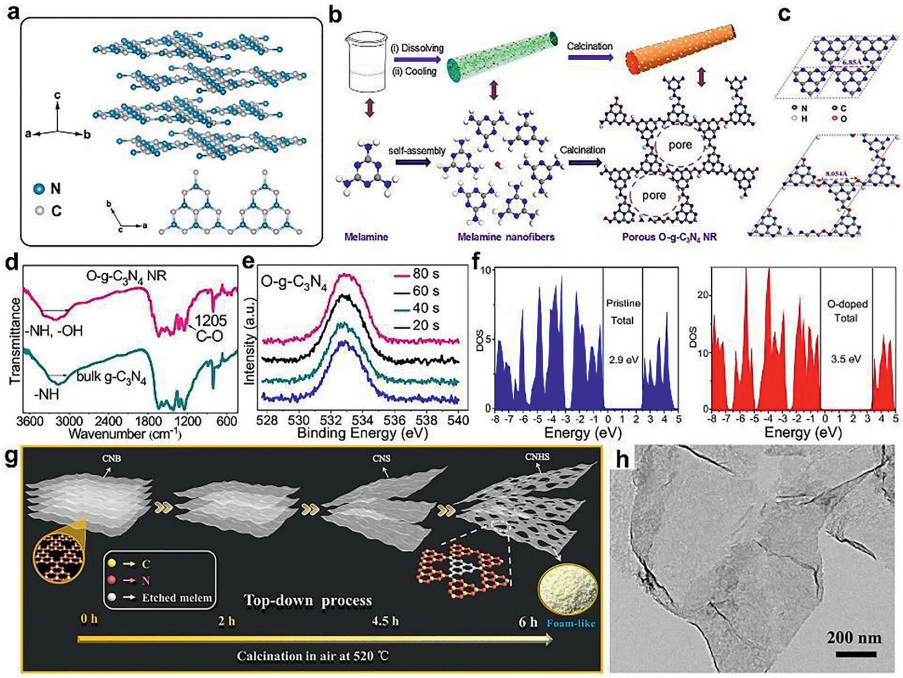

Fig. 9. (a) Crystal structure of g-C_3N_4. (b) Schematic illustration of *O*-g-C_3N_4 nanofibers formation. (c) Optimized structures of pristine g-C_3N_4 and *O*-g-C_3N_4. (d) FT-IR spectra of bulk g-C_3N_4 and *O*-g-C_3N_4. (e) The high-resolution XPS spectra upon Ar^+ splluttering of O. (f) Density of state (DOS) of pristine g-C_3N_4 (blue) and *O*-g-C_3N_4 nanofibers (red). Reprinted with permission [93]. Copyright 2018, Elsevier. (g) Top-down process for preparation of foam-like holey ultrathin g-C_3N_4 nanosheets. (h) TEM images of g-C_3N_4 nanosheets. Reprinted with permission [96]. Copyright 2016, Wiley-VCH.

to the larger specific surface area brought by the porous ultrathin structure, enhanced in-plane photo-generated carrier transfer, more exposed new edges and catalytic active site. In addition to calcination in air, argon or ammonia, liquid exfoliation is another typical preparation method that uses the chemical or physical effects of solvents (strong acid, methanol, formamide, *etc.*) and external forces (ultrasonic wave, pressure, thermal energy, *etc.*) to prepare 2D g-C_3N_4 nanosheets to improve the photocatalytic activity [97,98]. Combining g-C_3N_4 with other components to prepare nanocomposites is another effective strategy to improve the lifetime and transport efficiency of photogenerated charge carriers of g-C_3N_4 [99]. Based on the above-mentioned researches on 2D g-C_3N_4 nanosheets, the development of 2D/2D composites of g-C_3N_4 nanosheets and other 2D materials will provide favorable conditions for the high-efficiency charge transfer *via* large closely-connected interfaces in the photocatalytic process [100,101]. Putri *et al.* used the combined sonication-assisted electrostatic self-assembly method to hybridize positively-charged oxygen-doped g-C_3N_4 and negatively-charged boron-doped rGO to synthesize 2D-2D p-n heterojunction nanocomposites, which realized improved interfacial charge carrier transport and photocatalytic activity [102]. g-C_3N_4 is widely used in the environmental field due to its non-toxicity, simple synthesis, low cost and high stability. As a type of metal-free layered photocatalyst, more researches on g-C_3N_4 are devoted to interlayer doping and preparation of ultra-thin g-C_3N_4. In addition, the g-C_3N_4 nanosheets consist of tri-*s*-triazines interconnected by tertiary amines provide the structural feasibility for fabrication of g-C_3N_4-based composite nanomaterials. Benefiting from the above structural advantages, g-C_3N_4 will show broader application prospects in photocatalytic environmental purification.

3.2. Hexagonal boron nitride

Boron nitride (BN) composed of equal stoichiometric amounts of boron (B) and nitrogen (N) atoms has a variety of crystalline forms, such as hexagonal BN (h-BN), cubic BN (c-BN) and wurtzite BN (w-BN) [103,104]. Among them, h-BN as the stablest crystalline phase under ambient conditions has received the most attention. h-BN has a typical layered structure with the alternately linked B and N atoms within the layer by sp^2 hybridized B-N covalent bonds, and the 2D layers are held together by weak van der Waals forces (Fig. 10a) [105,106]. The metal-free h-BN nanomaterial has many unique physicochemical properties, such as low density, high stability, non-toxicity, *etc.*, which has been widely reported as a robust substrate for semiconductor photocatalysts [107]. In particular, when the bulk h-BN is exfoliated into 2D nanosheets, the negatively-charged h-BN nanosheets will attract photogenerated holes and improve the photoexcited charge carriers separation efficiency [108]. Limited by the wide band gap (5.5 eV to 6.0 eV) of h-BN, the researchers usually doped C and O to narrow the band gap and enhance photocatalytic activity [109,110]. Huang *et al.* synthesized sustainable and stable carbon-doped h-BN (BCN) nanosheets through a simple calcination method (Fig. 10b) [111]. The ternary BCN nanosheets showed outstanding photocatalytic performance for water splitting and CO_2 reduction, which can be attributed to the delocalized 2D electronic system formed by sp^2 carbon incorporation (Fig. 10c). Based on the layered structure of h-BN, the thin-layered h-BN as an excellent metal-free photocatalyst support or cocatalyst facilitates the homogeneous dispersion of semiconductor photocatalysts for improved photocatalytic performance. Liu *et al.* successfully prepared a novel porous BN/TiO_2 hybrid nanosheet by solvothermal method (Fig. 10d) [112]. Owing to the formation of B-O-Ti bond between the boron dangling bonds at the edges of the BN porous nanosheet structure and TiO_2 nanoparticles (Fig. 10e), the optimal porous BN/TiO_2 hybrid nanosheets (38 wt%) exhibited a photocatalytic degradation efficiency of 99% for Rhodamine B under visible light within 6h (Fig. 10f). In addition, the h-BN nanosheets can be combined with various 2D structures by layer-to-layer stacking, which can inherit the advantages of h-BN and hetero-components. Jiang *et al.* prepared h-BN/g-C_3N_4 metal-free heterojunction photocatalysts using an *in-situ* growth

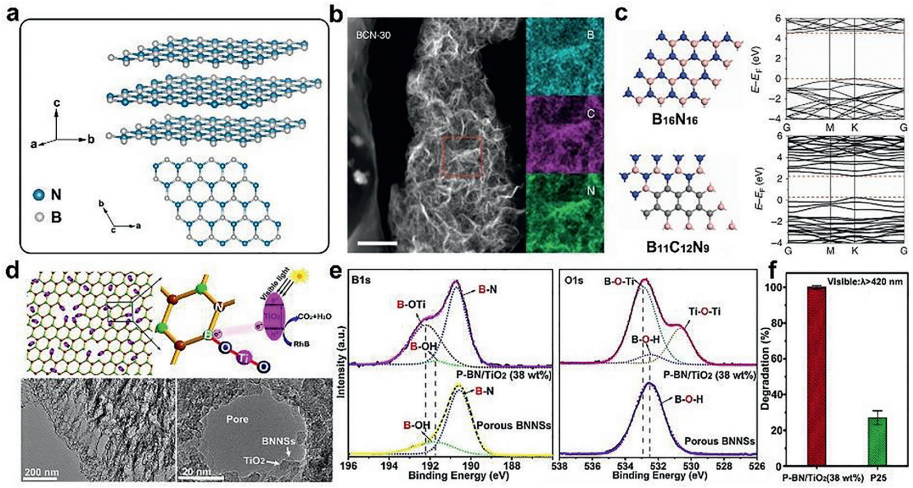

Fig. 10. (a) Crystal structure of h-BN. (b) Typical TEM dark-field image of BCN sample and the elemental mapping images of B, C and N of the enlargement of selected-area in the picture. Scale bar: 300 nm. (c) The optimized structure of $B_{16}N_{16}$ and $B_{11}C_{12}N_9$ with the corresponding calculated energy band. Reprinted with permission [111]. Copyright 2015, Nature. (d) Schematic diagram for the photocatalytic reaction of Rhodamine B by porous BN/TiO_2 hybrid nanosheets with new chemical bonding specie B-O-Ti under simulated visible light and TEM images for starting porous BN nanosheets and HRTEM images for a hole decorated by TiO_2 nanoparticles. (e) XPS spectra of B 1s, O 1s with porous and non-porous BN nanosheets, porous and non-porous BN/TiO_2 hybrid nanosheets. (f) Photodegradation of Rhodamine B under visible light $\lambda > 420$ nm by P25 and porous BN/TiO_2 hybrid nanosheets. Reprinted with permission [112]. Copyright 2017, Elsevier.

method [113]. The enhanced photocatalytic degradation activity of h-BN/g-C_3N_4 nanosheets is mainly attributed to the large specific surface area of the composite structure and the unique properties of h-BN as a photoexcited hole transfer promoter.

The layered h-BN nanosheets are called "white graphene" because of their similar crystal structure. In contrast to the huge progress made on carbon analogs, the researches on h-BN are quite limited. The wider band gap of h-BN limits its applicability in environmental and energy fields. The excellent performance of h-BN is mainly manifested by the extremely-high chemical stability, which makes it a promising photocatalyst support material. In addition, structural characteristics of h-BN still deserve attention, which will further promote the research on h-BN as a kind of promising metal-free solar-driven photocatalyst.

3.3. Black phosphorus

As one of the most abundant elements on earth, phosphorus has four allotropes: white, red, violet and black phosphorus. Among them, black phosphorus (BP) is the most thermodynamically stable allotrope due to its orthorhombic crystal structure [114]. Bulk BP is constructed by the single layer of phosphorus atoms (called phosphorene) with an interlayer spacing of 0.53 nm by weak van der Waals force [115]. This non-planar folded hexagonal structure consists of pleated phosphorus atoms connected by sp^3 hybrid covalent bonds, which is similar to the puckered honeycomb structure (Fig. 11a) [116].

As a strong competitor of graphene in photocatalytic applications, 2D black phosphorous has received extensive attention due to their adjustable band gap, strong light absorption, high charge mobility and large specific surface area. In 2014, Liu *et al.* used the tape micro-pyrolysis method for the first time to prepare a single-layer or a few-layer phosphorene [117]. Subsequently, the 2D BP was confirmed to be an outstanding catalyst for the conversion of solar energy to chemical energy in 2016 [118]. They prepared dispersed 2D BP flakes in *N*-methylpyrrolidone (NMP) under an inert atmosphere by the typical liquid exfoliation (Figs. 11b and c). The enhanced photocatalytic oxidation ability of 2D BP on triethylamine (TEA) was attributed to the increased band gap (from 0.3 eV to 2.1 eV), the promoted electron transfer, and the oxidative and reductive ability of photogenerated electrons and holes. Noteworthily, Wang *et al.* studied the subband structure of ultrathin BP nanosheets caused by low-dimensional many-body effects, which allowed BP nanosheets to possess optically switchable photocatalytic properties and light-dependent reactive oxygen species production ability (Fig. 11d) [119]. Compared with the bulk BP, ultrathin BP nanosheets generated singlet oxygen species ($^1O_2$) and $^{\bullet}OH$ under ultraviolet or visible light irradiation, respectively (Fig. 11e). The above-mentioned examples all showed that monolayers or few-layers of phosphorene exhibited outstanding photocatalytic performance. As a 2D material formed by van der Waals forces, the strategy for photocatalytic activity improvement of BP is focused on designing 2D/2D heterojunctions [120,121]. Ran *et al.* successfully prepared a new type of 2D/2D metal-free phosphorene/g-C_3N_4 van der Waals heterojunction through a simple self-assembly technology [122]. The 2D/2D heterostructure with a large interface area of phosphorene/g-C_3N_4 exhibited a 13-fold increase in solar energy conversion efficiency compared to primitive g-C_3N_4. The calculations of differential charge density proved that there is a strong electronic interaction between phosphorene and g-C_3N_4 nanosheets, which greatly improved the interfacial charge mobility (Fig. 11f). In addition, 2D phosphorene has massive reactive sites, which further contributed to enhanced photocatalytic activity.

As a direct band gap layered semiconductor, the band gap of BP can be adjusted from 2.0 eV to 0.3 eV by controlling the thickness, which demonstrated that BP has a wide range of optical absorption. The tunable bandgap and high hole mobility at room temperature make 2D BP more suitable for photocatalytic applications. In addition, fabrication of BP-based 2D/2D heterostructure can achieve enhanced separation of spatial photogenerated carriers through the large-area strong electronic coupling between the different phases. BP's unique structure and physicochemical properties make it expected to become the one of the most valuable materials in the post-graphene era.

4. Photocatalytic oxidation for environmental applications

Photocatalysis has been recognized as a potential advanced oxidation process (AOP) for effective water remediation and air purification using sunlight [123,124]. The layered photocatalytic materials have high expectations due to their unique structure, low cost,

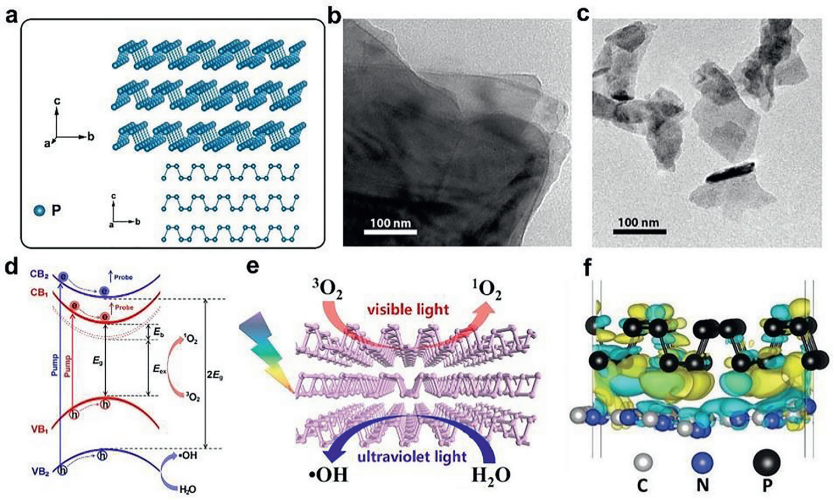

Fig. 11. (a) Crystal structure of BP. (b) Low resolution TEM image of bulk BP and (c) 2D BP. Reprinted with permission [118]. Copyright 2016, American Chemical Society. (d) Mechanism of photocatalytic reactive oxygen species generation over ultrathin BP nanosheet. (e) Schematic illustration of the subband structure of ultrathin BP nanosheet as well as the photoexcitation and photocatalytic processes occurring therein. Reprinted with permission [119]. Copyright 2018, American Chemical Society. (f) Side-view differential charge density map of g-C_3N_4 and phosphorene. Reprinted with permission [122]. Copyright 2018, Wiley-VCH.

non-toxicity and high oxidizing abilities in solar light [125]. Based on the characteristics of the layered structure, the 2D materials after exfoliation exhibit outstanding photooxidation activity [126]. In addition, the photooxidation ability of the photocatalysts can be further improved by appropriate strategies, such as morphological control, element doping, heterojunction construction [127].

4.1. Oxidation degradation of pollutants in water

Water pollution by pharmaceuticals and industrial pollutants and the search for effective strategies to deal with organic pollution are the main challenges that need to be resolved in the near future [128]. Till now, the applied wastewater treatment technologies mainly include biodegradation, chemical oxidation and electrochemical conversion, *etc.* [129,130]. However, in dealing with micropollutants that pose a huge threat to ecosystem, the above-mentioned methods are still not effective enough. With the advantages of low energy consumption and safety, photocatalytic technology has attracted more and more attention in the field of water remediation [131]. Ciprofloxacin (CIP) is a broad-spectral antibacterial agent commonly used for treating bacterial infections. The difficult degradation of CIP will lead to the increase of bacterial resistance, which seriously threatens human health [132]. Zeng *et al.* synthesized a bismuth oxybromide composite consisting of BiOBr and $Bi_{24}O_{31}Br_{10}$ phases by a simple solvothermal process with different additives including triethanolamine (TEOA), sodium hydroxide (NaOH) and ammonium hydroxide (NH_3 H_2O), which were named as S-TEOA, S-NaOH and S-NH_3, respectively (Fig. 12a) [133]. S-TEOA nanosheets with a high percentage of (001) facet of $Bi_{24}O_{31}Br_{10}$ had excellent adsorption properties and more surface oxygen vacancies, which resulted in efficient degradation of CIP under visible light irradiation (Fig. 12b). The adsorption mode of S-TEOA and CIP was uncovered as monodentate coordination and electrostatic interaction, which was conducive to the photogenerated charges at the interface to participate in the chemical reaction, thereby improving the photocatalytic degradation activity of the sample S-TEOA (Fig. 12c). As we well know, various active species such as $^{\bullet}OH$, photo-generated holes (h^+) and superoxide radical ($^{\bullet}O_2^-$) play an important role in the photocatalytic oxidation process of semiconductors. In this work, the adsorbed CIP was oxidized by photogenerated h^+, $^{\bullet}O_2^-$ and $^{\bullet}OH$ into final products including CO_2, H_2O, and small molecules (Eqs. 1–8).

$$O_2 + e^- \rightarrow {}^{\bullet}O_2^- \quad (1)$$

$$H_2O + h^+ \rightarrow {}^{\bullet}OH + H^+ + 2.27\ eV \quad (2)$$

$$OH^- + h^+ \rightarrow {}^{\bullet}OH + 2.38\ eV \quad (3)$$

$$2H^+ + O_2 + 2e^- \rightarrow H_2O_2 + 0.69\ eV \quad (4)$$

$$2H^+ + O_2 + e^- \rightarrow H_2O_2 + 1.71\ eV \quad (5)$$

$$H^+ + HO_2 + e^- \rightarrow H_2O_2 + 1.42\ eV \quad (6)$$

$$H_2O_2 + h\nu \rightarrow {}^{\bullet}OH + {}^{\bullet}OH \quad (7)$$

$$CIP + h^+ + {}^{\bullet}OH + {}^{\bullet}O_2^- \rightarrow CO_2 + H_2O + \text{small molecules} \quad (8)$$

4.2. Oxidation degradation/removal of air pollutants

With the rapid development of modern industry, air pollutants such as SO_x, NO_x and volatile organic compounds (VOC) become more and more serious and attract increasing attention [134]. For the removal of nitrogen oxides (NO_x) contributing to formation of photochemical smog, acid rain and tropospheric ozone in the air, a variety of technologies have been developed including electrochemical reduction and selective catalytic reduction, which can effectively remove high-concentration NO_x [135,136]. However, for the removal of low-concentration NO_x (NO and NO_2) at the ppb (parts per billion) level, photocatalysis is considered a promising green technology [137,138]. Wu *et al.* used electrostatic self-assembly technology to couple hollow porous carbon nitride nanospheres (HCNS) and reduced graphene oxide (rGO) to prepare HCNS/rGO metal-free heterojunction, which can remove NO in the air at 600 ppb level under visible light irradiation (Figs. 12d and e) [139]. The NO removal rate of the optimal sample reached 64% (Fig. 12f). In order to obtain more excellent photochemical stability and recyclability, HCNS/rGO was immobilized on C_3N_4 carbonized

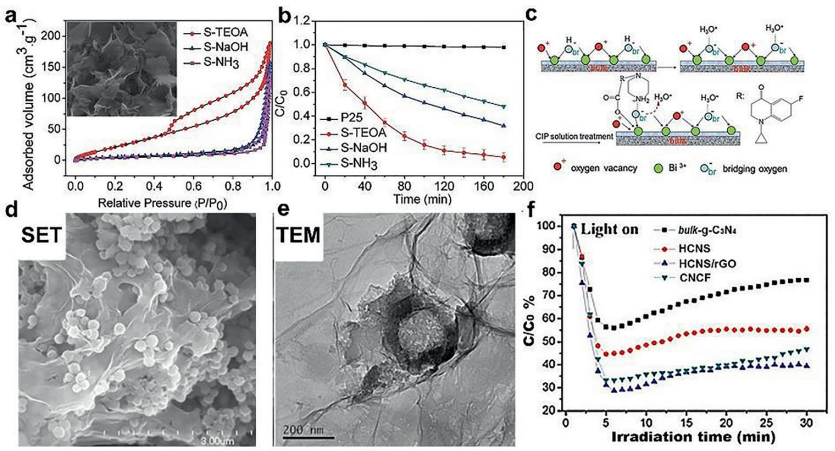

Fig. 12. (a) Nitrogen adsorption–desorption isotherms of the sample S-TEOA, S-NaOH and S-NH_3 (inset is SEM image of the S-TEOA). (b) Photocatalytic performance for CIP solution under visible light irradiation of CIP solution containing 150 mg of P25 and the samples S-TEOA, S-NaOH, S-NH_3. (c) Diagrammatic adsorption modes of CIP on the surface of the sample S-TEOA. Reprinted with permission [133]. Copyright 2017, Royal Society of Chemistry. (d) SEM and (e) TEM images of HCNS/rGO. (f) Visible-light photocatalytic performance of bulk-g-C_3N_4, HCNS, HCNS/rGO, and CNCF samples for the removal NO from air. Reprinted with permission [139]. Copyright 2016, Royal Society of Chemistry.

polymer nanofibers (CNCF) to form a photocatalytic film by electrospinning and carbonization. Furthermore, the photo-oxidation mechanism of photocatalytic removal of NO was given. HCNS/rGO generated reactive free radicals $^{\bullet}O_2^-$ and $^{\bullet}OH$ under visible light irradiation, which reacted with NO and produce HNO_2 and HNO_3. At the same time, holes also directly photo-oxidized NO to NO_3^-. The above processes can be described by the reaction shown in Eqs. 9–17.

$$HCNS/rGO + h\nu \rightarrow e^- + h^+ \quad (9)$$

$$e^- + O_2 \rightarrow {}^{\bullet}O_2^- \quad (10)$$

$$^{\bullet}O_2^- + 2H^+ + e^- \rightarrow H_2O_2 \quad (11)$$

$$H_2O_2 + e^- \rightarrow {}^{\bullet}OH + OH^- \quad (12)$$

$$NO + 2{}^{\bullet}OH \rightarrow NO_2 + H_2O \quad (13)$$

$$NO_2 + {}^{\bullet}OH \rightarrow NO_3^- + H^+ \quad (14)$$

$$NO + NO_2 + H_2O \rightarrow 2HNO_2 \quad (15)$$

$$NO + {}^{\bullet}O_2^- \rightarrow NO_3^- \quad (16)$$

$$NO_x + h^+ \rightarrow NO_3^- \quad (17)$$

More examples of photocatalytic oxidation for environmental applications have been provided in supporting documents (Figs. S1 and S2 in Supporting information).

5. Photocatalytic reduction for environmental applications

In artificial photocatalysis, photocatalytic reduction as the half-reaction of photocatalytic reaction also has an equally important position in environmental applications. In diversified photocatalytic reactions based on the strong reduction activity of layered photocatalysts, the CO_2 and Cr(VI) reduction have been paid intensive attentions [140,141].

5.1. Reduction of heavy metal pollutants

Heavy metal ions have the characteristics of strong toxicity, long half-life, easy accumulation in organisms and refractory degradation, *etc*. which mainly come from wastewater discharge of metallurgical industry, electroplate factory and nuclear industry. Photocatalytic technology as a potential solution has attracted extensive attention in the field of treating heavy metal pollutants including Cr(VI), Pb(II), Cu(II) and U(VI) in water due to its simplicity, non-toxicity, and high efficiency [142–145]. The photocatalytic mechanism is as follow (Eq. 18):

$$M^{n+} + e^- \rightarrow M \quad (18)$$

here, M^{n+} and M represent metal oxides and photocatalytic reduction products, respectively.

In industrial production, hexavalent chromium (Cr(VI)), as the common heavy metal pollutant, has attracted attention due to its high solubility and carcinogenicity [146,147]. The hexavalent chromium (Cr(VI)) and trivalent chromium (Cr(III)) exist in water as two stable oxidation states [148]. The strong toxicity of Cr(VI) makes it strictly limited in drinking water (0.05 mg/L), which is about 100 times that of Cr(III) [149]. Photoreduction of Cr(VI) to Cr(III) is considered to be an effective method for removing Cr(VI) from wastewater with low energy consumption [150,151]. However, the photoreduction process needs to be realized under acidic conditions [152]. Jia *et al.* designed a series of solid solutions $BiOBr_{1-x}I_x$ to dispose Cr(VI) over a wide range pH values by introducing iodine into BiOBr [153]. With pH ranging from 2 to 10, the removal rate of Cr(VI) remained at 98%, indicating that satisfactory synergistic effect of photoreduction and adsorption (Fig. 13a). The adsorption and photoreduction of Cr(VI) and the fixation process of Cr(III) under different pH values were proposed. Under acidic conditions, photoreduction dominates the removal of Cr(VI), which was described in the following Eqs. 19–21 (Figs. 13b and c).

$$14H^+ + Cr_2O_7^{2-} + 6e^- \rightarrow 2Cr^{3+} + 7H_2O \quad (19)$$

$$7H^+ + HCrO^{4-} + 3e^- \rightarrow Cr^{3+} + 4H_2O \quad (20)$$

$$CrO_4^{2-} + 4H_2O + 3e^- \rightarrow Cr(OH)_3(s) + 5OH^- \quad (21)$$

The strategy of substituting Br with I not only promoted the adsorption of Cr(VI) on $BiOBr_{0.25}I_{0.75}$, but also upshifted the CB

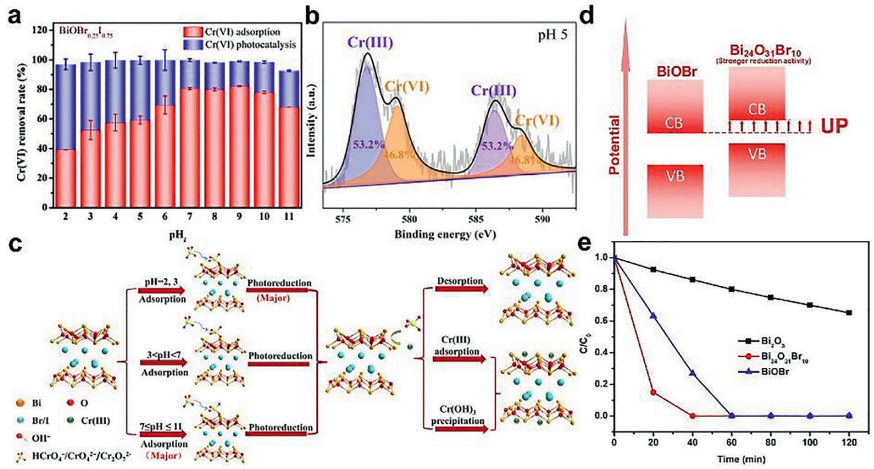

Fig. 13. (a) Effect of pH_i on the removal of Cr(VI) and (f) Cr(T) by $BiOBr_{0.25}I_{0.75}$. (b) High resolution of Cr 2p spectrum after photoreduction by $BiOBr_{0.25}I_{0.75}$ at pH 5. (c) Process for the removal of chromium on $BiOBr_{0.25}I_{0.75}$. Reprinted with permission [153]. Copyright 2021, Elsevier. (d) Schematic of the band gap structure of $BiOBr_{0.25}I_{0.75}$. (e) Comparison of photocatalytic activity for the Cr(VI) reduction experiment with Bi_2O_3, BiOBr, and $Bi_{24}O_{31}Br_{10}$. Reprinted with permission [154]. Copyright 2014, American Chemical Society.

position, enhancing the photoreduction ability for Cr(VI) to Cr(III). Similarly, Shang *et al*. successfully synthesized $Bi_{24}O_{31}Br_{10}$ with benign reduction activity by adjusting the proportions of Bi, O and Br (Fig. 13d) [154]. Compared with BiOBr, the $Bi_{24}O_{31}Br_{10}$ with the up-shifted CB bottom almost totally removed Cr(VI) within 40 min (Fig. 13e). More examples of photocatalytic reduction of heavy metal pollutants have been provided in supporting documents (Fig. S3).

5.2. Reduction of the organic pollutants

The photocatalytic degradation of organic pollutants can be divided into reduction by photogenerated electrons or oxidative degradation by holes and $^{\bullet}OH$ [155]. As a representative of organic pollutants, polybrominated diphenyl ethers (PBDEs) were classified as a persistent organic pollutant under the Stockholm Convention in 2012. Its degradation mechanism involves the widely studied photocatalytic reductive debromination. The photocatalytic reduction of PBDEs is usually carried out in anoxic solvents using selected sacrificial organic agents (such as methanol) [156], whereas photocatalytic oxidation is usually carried out in aqueous solutions [157]. More examples of photocatalytic reduction of the organic pollutants have been provided in supporting documents (Figs. S4a-c in Supporting information).

5.3. Reduction of NO_3^- and BrO_3^-

Managing the nitrogen cycle in water is one of the major challenges that society faces in the 21st century as identified by the National Society of Engineers. The use of nitrogen fertilizers in agriculture can lead to nitrate contamination of surface and groundwater. As an emerging transformation technology, photocatalytic nitrate reduction has attracted attention in the nitrate removal field to ensure the safety of drinking water resources [158]. The photocatalytic reduction of nitrate to nitrite, ammonium and nitrogen is described by Eqs. 22–24:

$$NO_3^- + 2H^+ + 2e^- \rightarrow NO_2^- + H_2O \quad (22)$$

$$NO_3^- + 10H^+ + 8e^- \rightarrow NH_4^+ + 3H_2O \quad (23)$$

$$2NO_3^- + 12H^+ + 10e^- \rightarrow N_2 + 6H_2O \quad (24)$$

Bromides naturally existing in surface water bodies are oxidized to bromate (BrO_3^-) in drinking water during disinfection processes such as ozonation, hypochlorination and chloramination. As another typical carcinogenic inorganic pollutant, it has been widely concerned. Photocatalytic technology is an effective strategy to remove BrO_3^-. During the photocatalytic reduction of BrO_3^-, the photogenerated electrons act as reducing species for BrO_3^- reduction (Eq. 25):

$$BrO_3^- + e^- + 6H^+ \rightarrow Br^- + 3H_2O \quad (25)$$

More examples of photocatalytic reduction of NO_3^- and BrO_3^- have been provided in supporting documents (Figs. S4d-f in Supporting information).

5.4. CO_2 reduction

Global warming is increasing year by year, which is caused by the large amount of CO_2 gas emitted from the burning of fossil fuels [159,160]. In addition to decreasing the fossil fuel consumption, the development of clean, efficient and renewable green technologies is urgently needed to convert excess CO_2 into valuable products [161]. Semiconductor photocatalytic CO_2 reduction provides a strategy to kill two birds with one stone, which solves the problems of greenhouse effect and energy crisis at the same time. In this system, the photocatalysts convert solar energy into chemical energy, that is, reducing CO_2 to valuable compounds, such as carbon monoxide, methane, methanol, and ethanol [162,163]. The CO_2 reduction capability is related to the energy band position of photocatalysts [164]. The bottom of the conduction band of photocatalysts must be more negative than the reduction potential of various reduction products of CO_2, which are listed in Eqs. 26–30.

$$CO_2 + 2H^+ + 2e^- \rightarrow HCOOH, E^0 = -0.61\ V \quad (26)$$

$$CO_2 + 2H^+ + 2e^- \rightarrow CO + H_2O, E^0 = -0.53\ V \quad (27)$$

$$CO_2 + 4H^+ + 4e^- \rightarrow HCHO + H_2O, E^0 = -0.48\ V \quad (28)$$

$$CO_2 + 6H^+ + 6e^- \rightarrow CH_3OH + H_2O, E^0 = -0.38\ V \quad (29)$$

$$CO_2 + 8H^+ + 8e^- \rightarrow CH_4 + H_2O, E^0 = -0.24\ V \quad (30)$$

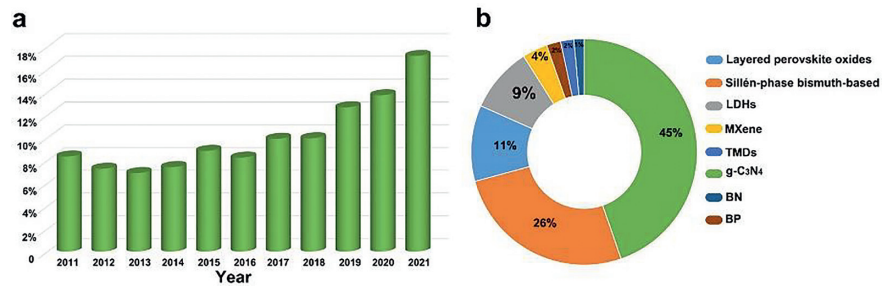

Fig. 14. (a) The results for number of publications on photocatalysis for environmental applications and the share of literature on layered photocatalytic nanomaterials among them from 2011 to 2021. (b) The proportion of photocatalysts for each search query in the number of publications on layered photocatalytic nanomaterials. Date from Web of Science (WOS).

Therefore, band structure engineering is one of the effective strategies to control the selectivity of CO_2 reduction products [165]. More examples of photocatalytic CO_2 reduction have been provided in supporting documents (Fig. S5 in Supporting information).

6. Summary and outlook

A gradual increase in the proportion of layered photocatalysts has been observed from published articles related to the field of photocatalytic environmental applications in the last decade (by WOS) (Fig. 14a), indicating that layered photocatalytic nanomaterials as one of the promising material families, have received more and more attention due to their high efficiency and rich tunability in structure and property. The structure of the layered materials consisting of stacked sheets enables many interesting design and modification possibilities, such as the tailorable nanostructure, controllable accessibility to sites and characteristics, adjustable pore structure and specific surface area.

For all layered photocatalytic nanomaterials that have been reviewed, g-C_3N_4 gave the maximum number of search results compared to other photocatalysts, followed by Sillén-phase bismuth-based photocatalysts represented by BiOX (X = Cl, Br and I, Fig. 14b). The burgeoning expansion study of nanoscale layered g-C_3N_4 and BiOX photocatalysts over the past decade has indisputably witnessed unique properties with extraordinary ameliorated photocatalytic applications in environmental remediation. Especially as a metal-free semiconductor photocatalyst, g-C_3N_4 has become the research hotspot for pollutant photodegradation, reduction of high-valent metal ions and greenhouse gases due to its unique layered structure and simple modification methods. For the selection of the modification strategies, in addition to considering the structural characteristics of the material itself, the mechanism exploration of the whole photocatalytic process will also provide the accurate guides for the development of efficient layered photocatalysts with high stability and activity. Compared with the photocatalytic reduction process utilizing photogenerated electrons, the multi-step mechanisms of photocatalytic oxidative degradation are that holes oxidize water molecules to generate $^{\bullet}OH$ or directly act on pollutants. In addition, the anionic $^{\bullet}O_2^-$ generated from the reduction of adsorbed oxygen molecules by photogenerated electrons also have strong oxidizing properties. Meanwhile, the protonation of superoxide will generate hydroperoxide radicals, hydrogen peroxide and eventually form $^{\bullet}OH$ radicals. It is worth noting that the non-selective pollutant treatment degree depends not only on the photocatalytic performance, but also depends on the structural stability of the degradation products. Therefore, the molecular-level assessment of the photocatalytic process is of immeasurable significance for the development of efficient photocatalytic materials for environmental purification.

This review summarizes the basic knowledge of the layered photocatalytic nanomaterials based on their classification, structure and composition, the modification strategy for optimizing the photocatalytic efficiency in environmental field, and the overall development status of layered photocatalytic materials. Although significant progress has been made in layered photocatalytic materials in the purification of water and air pollutants, there are still challenges in current small-scale photocatalytic research, which is far from practical applications. In general, it is very necessary to explore the correlation among photocatalyst activity, involved reaction mechanism and the structural properties of photocatalysts at the micro-atomic scale, which will depend on the development of more *in-situ* characterization techniques. Based on the mastery of the above-mentioned laws, in addition to focusing on high photocatalytic activity, the durability of the photocatalytic environmental treatment system should also be paid more attention to ensure industrial-grade long-term stability. In addition, the ideal photocatalyst needs to consider the economic benefits of industrial scale. Therefore, it is very important to develop the photocatalyst composed of abundant elements on the earth with high stability, scalability and excellent photocatalytic activity. Meanwhile, the strong collaboration between materials science and engineering is required to achieve best consequences.

A clean environment is the basic requirement to maintain the sustainable development of life on earth. The photocatalytic technology is committed to solving environmental pollution problems in a greener way. A large number of reports on layered photocatalytic materials have proven their potential in environmental applications. There is no doubt that layered photocatalytic nanomaterials will be explored in more detail to meet scalability requirements and solve global environmental problems.

Declaration of competing interest

The authors declare that they have no known competing financial interests or personal relationships that could have appeared to influence the work reported in this paper.

Acknowledgments

This work was jointly supported by the National Natural Science Foundation of China (Nos. 51972288 and 51672258), the Fundamental Research Funds for the Central Universities (No. 2652018287).

Supplementary materials

Supplementary material associated with this article can be found, in the online version, at doi:10.1016/j.cclet.2022.05.037.

References

[1] D. O'Connor, D.Y. Hou, Y.S. Ok, et al., J. Controlled Release 283 (2018) 200–213.

[2] S. Mukherjee, U. RoyChaudhuri, P.P. Kundu, J. Chem. Technol. Biotechnol. 93 (2018) 1300–1311.
[3] Y. Yang, Y.S. Ok, K. Kim, E.E. Kwon, Y.F. Tsang, Sci. Total Environ. 596 (2017) 303–320.
[4] Z. Shayegan, C. Lee, F. Haghighat, Chem. Eng. J. 334 (2018) 2408–2439.
[5] S.B. Wang, X. Han, Y.H. Zhang, et al., Small Struct. (2021) 2000061.
[6] W.S. Koe, J.W. Lee, W.C. Chong, Y.L. Pang, L.C. Sim, Environ. Sci. Pollut. Res. 27 (2020) 2522–2565.
[7] S. Huang, T. Ouyang, B. Zheng, M. Dan, Z. Liu, Angew. Chem. Int. Ed. 60 (2021) 9546–9552.
[8] S. Huang, B. Zheng, Z. Tang, et al., Chem. Eng. J. 422 (2021) 130086.
[9] A. Fujishima, K. Honda, Nature 238 (1972) 37–38.
[10] Q. Guo, C.Y. Zhou, Z.B. Ma, X.M. Yang, Adv. Mater. 31 (2019) 1901997.
[11] D.Q. Zhang, G.S. Li, H.X. Li, Y.F. Lu, Chem. Asian J. 8 (2013) 26–40.
[12] W. Yang, H. Wang, R. Liu, et al., Angew. Chem. Int. Ed. 60 (2021) 409–414.
[13] S. He, C. Yan, X. Chen, et al., Appl. Catal. B 276 (2020) 119138.
[14] Y.B. Chen, J. Li, P. Liao, et al., Chin. Chem. Lett. 31 (2020) 1516–1519.
[15] B.C. Zhu, B. Cheng, J.J. Fan, W. Ho, J.G. Yu, Small Struct. 2 (2021) 2100086.
[16] Y.L. Zhu, W. Zhou, Z.P. Shao, Small 13 (2017) 1603793.
[17] G. Zhang, G. Liu, L.Z. Wang, J.T. Irvine, Chem. Soc. Rev. 45 (2016) 5951–5984.
[18] Y.C. Hu, L.H. Mao, X.J. Guan, et al., Renew. Sust. Energy Rev. 119 (2020) 109527.
[19] H. Wang, Y.H. Liang, L. Liu, J.S. Hu, W.Q. Cui, Appl. Surf. Sci. 392 (2017) 51–60.
[20] S.G. Li, L.Q. Bai, N. Ji, et al., J. Mater. Chem. A 8 (2020) 9268–9277.
[21] H.J. Yu, H.W. Huang, A.H. Reshak, et al., Appl. Catal. B 284 (2021) 119709.
[22] A. Kumar, A. Kumar, V. Krishnan, ACS Catal. 10 (2020) 10253-10315.
[23] Y.G. Ko, W.Y. Lee, Catal. Lett. 83 (2020) 157–160.
[24] A.L. Sorkh-Kaman-Zadeh, A. Dashtbozorg, J. Mol. Liq. 223 (2016) 921–926.
[25] Y. Tao, L. Wu, X.L. Zhao, et al., ACS Appl. Mater. Interfaces 11 (2019) 25967–25975.
[26] K.D. Wang, H.S. Li, X.L. Chen, et al., Mater. Lett. 220 (2018) 54–57.
[27] Y.C. Hu, L.H. Mao, X.J. Guan, et al., Renew. Sust. Energy Rev. 119 (2020) 109527.
[28] K. Iizuka, T. Wato, Y. Miseki, K.J. Saito, A. Kudo, J. Am. Chem. Soc. 133 (2011) 20863–20868.
[29] Y.S. Ebina, N. Sakai, J. Phys. Chem. B 109 (2005) 17212–17216.
[30] A. Mukherji, C.H. Sun, S.C. Smith, G.Q. Lu, L.Z. Wang, J. Phys. Chem. C 115 (2011) 15674–15678.
[31] A. Mukherji, B. Seger, G.Q. Lu, L.Z. Wang, ACS Nano 5 (2011) 3483–3492.
[32] M.L. Guan, C. Xiao, J. Zhang, et al., J. Am. Chem. Soc. 135 (2013) 10411–10417.
[33] Y.Y. Wu, H.D. Ji, Q.M. Liu, et al., J. Hazard. Mater. 424 (2022) 127563.
[34] J. Jiang, K. Zhao, X.Y. Xiao, L.Z. Zhang, J. Am. Chem. Soc. 134 (2012) 4473–4476.
[35] M.L. Pan, H.J. Zhang, G.D. Gao, L. Liu, W. Chen, Environ. Sci. Technol. 49 (2015) 6240–6248.
[36] Y.X. Guo, I. Siretanu, Y.H. Zhang, et al., J. Mater. Chem. A 6 (2018) 7500–7508.
[37] M. Shi, G.N. Li, J.M. Li, et al., Angew. Chem. Int. Ed. 132 (2020) 6652–6657.
[38] D. Wu, B. Wang, W. Wang, et al., J. Mater. Chem. A 3 (2015) 15148–15155.
[39] M. Li, S.X. Yu, H.W. Huang, et al., Angew. Chem. Int. Ed. 58 (2019) 9517–9521.
[40] J. Li, Y. Yu, L.Z. Zhang, Nanoscale 6 (2014) 8473–8488.
[41] J. Li, L.J. Cai, J. Shang, Y. Yu, L.Z. Zhang, Adv. Mater. 28 (2016) 4059–4064.
[42] H. Wang, D.Y. Yong, S.C. Chen, et al., J. Am. Chem. Soc. 140 (2018) 1760–1766.
[43] H.W. Huang, S.C. Tu, C. Zeng, et al., Angew. Chem. Int. Ed. 56 (2017) 11860–11864.
[44] F. Chen, Z.Y. Ma, L.Q. Ye, et al., Adv. Mater. 32 (2020) 1908350.
[45] Y. Zheng, F. Duan, M.Q. Chen, Y. Xie, J. Mol. Catal. A: Chem. 317 (2010) 34–40.
[46] Z.Y. Zhao, Y. Zhou, F. Wang, et al., ACS Appl. Mater. Interfaces 7 (2015) 730–737.
[47] Q.T. Zhang, S.S. Yuan, B. Xu, et al., Catal. Today 315 (2018) 184–193.
[48] H. Fujito, H. Kunioku, D.C. Kato, H. Kageyama, R. Abe, J. Am. Chem. Soc. 138 (2016) 2082–2085.
[49] Y. You, S.B. Wang, K. Xiao, et al., ACS Sustain. Chem. Eng. 6 (2018) 16219–16227.
[50] K.T. Ogawa, A. Nakada, A. Saeki, H. Kageyama, R. Abe, ACS Appl. Mater. Interfaces 11 (2018) 5642–5650.
[51] C. Hu, H.W. Huang, F. Chen, et al., Adv. Funct. Mater. 30 (2020) 1908168.
[52] X. Xiang, F. Li, Z.Q. Huang, Rev. Adv. Sci. Eng. 3 (2014) 158–171.
[53] S.J. Xia, L.Y. Zhang, X.B. Zhou, G.X. Pan, Z.M. Ni, Appl. Clay Sci. 114 (2015) 577–585.
[54] J. Das, K. Parida, J. Mol. Catal. A: Chem. 264 (2007) 248–254.
[55] G.H. Zhang, X.Q. Zhang, Y. Meng, et al., Chem. Eng. J. 392 (2020) 123684.
[56] L. Mohapatra, K. Parida, J. Mater. Chem. A 4 (2016) 10744–10766.
[57] T. Subramanian, A. Dhakshinamoorthy, K.S. Pitchumani, Tetrahedron Lett. 54 (2013) 7167–7170.
[58] G.X. Chen, S.M. Qian, X.M. Tu, et al., Appl. Surf. Sci. 293 (2014) 345–351.
[59] B. Li, Y.F. Zhao, S.T. Zhang, W. Gao, M. Wei, ACS Appl. Mater. Interfaces 5 (2013) 10233–10239.
[60] J.L. Gunjakar, T.W. Kim, H.N. Kim, I.Y. Kim, S. Hwang, J. Am. Chem. Soc. 133 (2011) 14998–15007.
[61] K. Hantanasirisakul, Y. Gogotsi, Adv. Mater. 30 (2018) 1804779.
[62] J.X. Nan, X. Guo, J. Xiao, et al., Small 17 (2021) 1902085.
[63] Y.L. Sun, X. Meng, Y.H. Dall'gnese, et al., Nano-Micro Lett. 11 (2019) 79.
[64] X.D. Sun, H.W. Huang, Q. Zhao, T.Y. Ma, L.Z. Wang, Adv. Funct. Mater. 30 (2020) 1910005.
[65] X.H. Wu, Z.Y. Wang, M.Z. Yu, L.Y. Xiu, J.S. Qiu, Adv. Mater. 29 (2017) 1607017.
[66] T. Cai, L.L. Wang, Y.T. Liu, et al., Appl. Catal. B 239 (2018) 545–554.
[67] S.W. Cao, B.J. Shen, T. Tong, J.W. Fu, J.G. Yu, Adv. Funct. Mater. 28 (2018) 1800136.
[68] B. Balasubramaniam, N. Singh, P. Kar, et al., Mol. Syst. Des. Eng. 4 (2019) 804–827.
[69] R.T. Lv, J.A. Robinson, R.E. Schaak, et al., Acc. Chem. Res. 48 (2015) 56–64.
[70] H. Ramakrishna Matte, A. Gomathi, A.K. Manna, et al., Angew. Chem. Int. Ed. 49 (2010) 4059–4062.
[71] X.M. Guo, J.Y. Ji, Q.G. Jiang, et al., ACS Appl. Mater. Interfaces 9 (2017) 30591–30598.
[72] A.L. Jawaid, D. Nepal, K. Park, et al., Chem. Mater. 28 (2016) 337–348.
[73] G. Koyyada, S.P. Vattikuti, J. Shim, V. Chitturi, J.H. Jung, Mater. Res. Bull. 109 (2019) 246–254.
[74] X. Zong, H.J. Yan, G.P. Wu, et al., J. Am. Chem. Soc. 130 (2008) 7176–7177.
[75] W. Peng, X. Wang, X. Li, Nanoscale 6 (2014) 8311–8317.
[76] S.P. Vattikuti, C. Byon, C.V. Reddy, R. Ravikumar, RSC Adv. 5 (2015) 86675-86684.
[77] S.E. Islam, D. Hang, C. Chen, K.H. Sharma, Chem. Eur. J. 24 (2018) 9305–9315.
[78] W.C. Peng, Y. Li, F.B. Zhang, G.L. Zhang, X.B. Fan, Ind. Eng. Chem. Res. 56 (2017) 4611–4626.
[79] S.Y. Guo, H.H. Luo, Y. Li, et al., J. Alloys Compd. 852 (2021) 157026.
[80] E.C. Franklin, J. Am. Chem. Soc. 44 (1922) 486–509.
[81] X.C. Wang, S. Blechert, M. Antonietti, ACS Catal. 2 (2012) 1596–1606.
[82] X.C. Wang, K. Maeda, A. Thomas, et al., Nat. Mater. 8 (2009) 76–80.
[83] X.L. Liu, R. Ma, L. Zhuang, et al., Crit. Rev. Environ. Sci. Technol. 51 (2021) 751–790.
[84] Q. Hao, G.H. Jia, W. Wei, et al., Nano Res. 13 (2020) 18–37.
[85] J.J. Zhu, P. Xiao, H.L. Li, S.A. Carabineiro, ACS Appl. Mater. Interfaces 6 (2014) 16449–16465.
[86] J. Jiang, S.W. Cao, C.L. Hu, C.H. Chen, Chin. J. Catal. 38 (2017) 1981–1989.
[87] S.Z. Hu, F.Y. Li, Z.P. Fan, et al., Dalton Trans 44 (2015) 1084–1092.
[88] Z. Li, C. Kong, G.X. Lu, J. Phys. Chem. C 120 (2016) 56–63.
[89] L. Muniandy, F. Adam, A.R. Mohamed, A. Iqbal, Appl. Surf. Sci. 398 (2017) 43–55.
[90] L. Zhou, H.Y. Zhang, H.Q. Sun, et al., Catal. Sci. Technol. 6 (2016) 7002–7023.
[91] T. Xiong, W.L. Cen, Y.X. Zhang, F. Dong, ACS Catal. 6 (2016) 2462–2472.
[92] Z. Huang, J.J. Song, L. Pan, et al., Nano Energy 12 (2015) 646–656.
[93] Y.X. Zeng, X. Liu, C.B. Liu, et al., Appl. Catal. B 224 (2018) 1–9.
[94] C. Hu, F. Chen, Y.G. Wang, et al., Adv. Mater. 33 (2021) 2101751.
[95] C.Z. Wu, S.Y. Xue, Z.J. Qin, et al., Appl. Catal. B 282 (2021) 119557.
[96] Y.F. Li, R.X. Jin, Y. Xing, et al., Adv. Energy Mater. 6 (2016) 1601273.
[97] N. Bao, X.D. Hu, Q.Z. Zhang, et al., Appl. Surf. Sci. 403 (2017) 682–690.
[98] L.J. Fang, Y.H. Li, P.F. Liu, et al., ACS Sustain. Chem. Eng. 5 (2017) 2039–2043.
[99] F. Ding, D. Yang, Z.W. Tong, et al., Environ. Sci. Nano 4 (2017) 1455–1469.
[100] B.J. Sun, W. Zhou, H.Z. Li, et al., Adv. Mater. 30 (2018) 1804282.
[101] J.X. Low, B.Z. Dai, T. Tong, C.J. Jiang, J.G. Yu, Adv. Mater. 31 (2019) 1802981.
[102] L.K. Putri, B. Ng, W. Ong, et al., J. Mater. Chem. A 6 (2018) 3181–3194.
[103] N.S. Mishra, P. Saravanan, ChemistrySelect 3 (2018) 8023–8034.
[104] Q.H. Weng, X.B. Wang, X. Wang, D. Golberg, Chem. Soc. Rev. 45 (2016) 3989–4012.
[105] W. Luo, Y.B. Wang, E. Hitz, et al., Adv. Funct. Mater. 27 (2017) 1701450.
[106] S.J. Yu, X.X. Wang, H.W. Pang, et al., Chem. Eng. J. 333 (2018) 343–360.
[107] Q.H. Weng, X.B. Wang, X. Wang, D. Golberg, Chem. Soc. Rev. 45 (2016) 3989–4012.
[108] S.G. Meng, X.J. Ye, X.F. Ning, et al., Appl. Catal. B 182 (2016) 356–368.
[109] J.Q. Li, N. Lei, H.J. Hao, J. Zhou, Chem. Phys. Lett. 672 (2017) 99–104.
[110] R. Sevak Singh, R. Yingjie Tay, W. Leong Chow, et al., Appl. Phys. Lett. 104 (2014) 163101.
[111] C.J. Huang, C. Chen, M.W. Zhang, et al., Nat. Commun. 6 (2015) 7698.
[112] D. Liu, M.W. Zhang, W.J. Xie, et al., Appl. Catal. B 207 (2017) 72–78.
[113] L.B. Jiang, X.Z. Yuan, G.M. Zeng, et al., Appl. Catal. B 221 (2018) 715–725.
[114] B.S. Li, C. Lai, G.M. Zeng, et al., Small 15 (2019) 1804565.
[115] T. Sakthivel, X.Y. Huang, Y.C. Wu, S.M. Rtimi, Chem. Eng. J. 379 (2020) 122297.
[116] A. Castellanos-Gomez, L. Vicarelli, E. Prada, et al., 2D Mater. 1 (2014) 025001.
[117] H. Liu, A.T. Neal, Z. Zhu, et al., ACS Nano 8 (2014) 4033–4041.
[118] J. Hu, Z.K. Guo, P.E. Mcwilliams, et al., Nano Lett. 16 (2016) 74–79.
[119] H. Wang, S.L. Jiang, W. Shao, et al., J. Am. Chem. Soc. 140 (2018) 3474–3480.
[120] J.J. Wang, L. Tang, G.M. Zeng, et al., Appl. Catal. B 209 (2017) 285–294.
[121] M.S. Zhu, C.Y. Zhai, T. Majima, Appl. Catal. B 221 (2018) 645–651.
[122] J.R. Ran, W.W. Guo, H.L. Wang, et al., Adv. Mater. 30 (2018) 1800128.
[123] H. Zhong, Z.Q. Wang, Z.F. Liu, et al., Int. Biodeterior. Biodegrad. 115 (2016) 141–145.
[124] Y. Liu, M. Cheng, Z.F. Liu, et al., Chemosphere 236 (2019) 124387.
[125] G. Centi, S. Perathoner, Microporous Mesoporous Mater. 107 (2008) 3–15.
[126] J.X. Low, S.W. Cao, J.G. Yu, S. Wageh, Chem. Commun. 50 (2014) 10768–10777.
[127] H.J. Li, Y. Zhou, W. Tu, J.H. Ye, Z.G. Zou, Adv. Funct. Mater. 25 (2015) 998–1013.
[128] S. Giannakis, S.M. Rtimi, C. Pulgarin, Molecules 22 (2017) 1070.
[129] I.M. Bulai, J. Math. Chem. 54 (2016) 1387–1403.
[130] Y.J. Yao, H. Chen, C. Lian, et al., J. Hazard. Mater. 314 (2016) 129–139.
[131] W. Zhang, Z.T. Zeng, Z.F. Liu, et al., Ecotoxicol. Environ. Saf. 189 (2020) 109914.
[132] T. Paul, P.L. Miller, T.J. Strathmann, Environ. Sci. Technol. 41 (2007) 4720–4727.
[133] X.X. Zeng, Y.Q. Wan, X.F. Gong, Z.D. Xu, RSC Adv. 7 (2017) 36269–36278.
[134] M.Z. Jacobson, Energy Environ. Sci. 2 (2009) 148–173.
[135] I. Heo, M.K. Kim, S. Sung, et al., Environ. Sci. Technol. 47 (2013) 3657–3664.
[136] J. Lasek, Y. Yu, J.C. Wu, J. Photochem. Photobiol. C 14 (2013) 29–52.
[137] G.H. Dong, W. Ho, L.Z. Zhang, Appl. Catal. B 168 (2015) 490–496.
[138] Y. Bai, P. Yang, P.Q. Wang, et al., J. Taiwan Inst. Chem. Eng. 82 (2018) 273–280.

[139] H.X. Wu, D.Y. Chen, N.J. Li, et al., Nanoscale 8 (2016) 12066–12072.
[140] S. Lingampalli, M.M. Ayyub, C. Rao, ACS Omega 2 (2017) 2740–2748.
[141] Z.Y. Zhao, H. An, J. Lin, et al., Chem. Rec. 19 (2019) 873–882.
[142] S.Q. Huang, T. Ouyang, J.Y. Chen, et al., J. Colloid Interface Sci. 605 (2022) 602–612.
[143] Y.N. Liu, Z.F. Shen, J.L. Song, et al., Chin. Chem. Lett. 31 (2020) 2747–2751.
[144] K. Kabra, R. Sawhney, J. Hazard. Mater. 149 (2007) 680–685.
[145] Y.X. Ye, P. Yang, Y.W. Deng, et al., Chin. Chem. Lett. 33 (2022) 3127–3132.
[146] D.D. Wang, Y.G. Xu, M. Xie, et al., J. Hazard. Mater. 384 (2020) 121480.
[147] A.L. Jin, X. Liu, M.R. Li, et al., ACS Sustain. Chem. Eng. 7 (2019) 5122–5133.
[148] H. Wu, C. Chang, D.L. Lu, K. Maeda, ACS Appl. Mater. Interfaces 11 (2019) 35702–35712.
[149] H. Sereshti, M.V. Farahani, M. Baghdadi, Talanta 146 (2016) 662–669.
[150] C.M. Li, G. Chen, J.X. Sun, et al., Appl. Catal. B 188 (2016) 39–47.
[151] J. Zhang, N. Gao, F.L. Chen, et al., Chem. Eng. J. 358 (2019) 398–407.
[152] B. Valizadeh, T.N. Nguyen, S. Kampouri, et al., J. Mater. Chem. A 8 (2020) 9629–9637.
[153] L.X. Jia, X. Tan, Y.F. Li, et al., Chin. Chem. Lett. 33 (2022) 3053–3060.
[154] J. Shang, W.C. Hao, X.J. Lv, et al., ACS Catal. 4 (2014) 954–961.
[155] D.C. Schmelling, K.A. Gray, P.V. Kamat, Environ. Sci. Technol. 30 (1996) 2547–2555.
[156] Y. Shao, W. Ye, C. Sun, C. Liu, Q. Wang, RSC Adv. 7 (2017) 39089-39095.
[157] A.Z. Huang, N. Wang, M. Lei, et al., Environ. Sci. Technol. 47 (2013) 518–525.
[158] H.O. Tugaoen, S. Garcia-Segura, K. Hristovski, P. Westerhoff, Sci. Total Environ. 599 (2017) 1524–1551.
[159] S.I. Seneviratne, J. Rogelj, R. Seferian, et al., Nature 558 (2018) 41–49.
[160] J. Goldemberg, Science 315 (2007) 808–810.
[161] W.L. Abou Saoud, A.A. Assadi, M.N. Guiza, et al., Appl. Catal. B 213 (2017) 53–61.
[162] N. Kornienko, J.Z. Zhang, K.K. Sakimoto, P.D. Yang, E. Reisner, Nat. Nanotechnol. 13 (2018) 890–899.
[163] J.F. Shi, Y.J. Jiang, Z.Y. Jiang, et al., Chem. Soc. Rev. 44 (2015) 5981–6000.
[164] N. Vu, S. Kaliaguine, T. Do, Adv. Funct. Mater. 29 (2019) 1901825.
[165] C. Zeng, H.W. Huang, T.R. Zhang, et al., ACS Appl. Mater. Interfaces 9 (2017) 27773–27783.